Geophysical Journal International

Geophys. J. Int. (2014) **197,** 748–767
Advance Access publication 2014 March 25

doi: 10.1093/gji/ggu075

Seismic imaging of crust beneath the Dharwar Craton, India, from ambient noise and teleseismic receiver function modelling

Kajaljyoti Borah,[1] S. S. Rai,[1] K. S. Prakasam,[1] Sandeep Gupta,[1] Keith Priestley[2] and V. K. Gaur[3]

[1]*CSIR-National Geophysical Research Institute, Uppal Road, Hyderabad* 500007, *India. E-mail: kajalborah1979@gmail.com*
[2]*Bullard Laboratories, University of Cambridge, CB*3 0*EZ, United Kingdom*
[3]*Indian Institute of Astrophysics, Bangalore* 560034, *India*

Accepted 2014 February 25. Received 2014 February 25; in original form 2013 September 28

SUMMARY

We use cross-correlation of continuous 18 months (2009 February to 2010 August) ambient noise data recorded over 35 broad-band seismographs in the Archean Dharwar Craton and the adjoining granulite terrain to generate Rayleigh-wave group velocity maps in the period 5–28 s. This is supplemented with longer period data (40–70 s) from earthquake source. Combined group velocity measurement was inverted jointly with the teleseismic receiver functions obtained at 50 stations (includes 15 stations operated during 1998–2002) to produce shear velocity image of the crust. The velocity image reveals thinner crust (34–38 km) in the late Archean (∼2.7 Ga) Eastern Dharwar Craton (EDC), while all other terrains (mid-Archean and Proterozoic) have crustal thickness from 40 to over 50 km. The mid-Archean (3.36 Ga) greenstone belt of the Western Dharwar Craton (WDC) has the thickest crust (∼50 km). The average crustal V_s beneath the EDC is ∼3.70–3.78 km s^{-1} as compared to 3.80–3.95 km s^{-1} beneath the WDC. We observe significant lateral variation in the thickness of lower crust (V_s ∼ 3.8–4.2 km s^{-1}): ∼10–15 km in the EDC compared to ∼20–30 km in the WDC. The lowermost part of the crust ($V_s \geq 4.0$ km s^{-1}) is thin (<5 km) beneath the EDC in contrast to more thickness (10–27 km) beneath the WDC. Our analysis suggests intermediate composition for the crust beneath the EDC similar to those for other cratons. In contrast, the mid-Archean exposed WDC crust has more mafic composition and exceptional thickness—a scenario at variance with the global observations. We interpret this thick mafic crust to represent undeformed geological segment of 3.36 Ga. The EDC with a nearly flat Moho, felsic to intermediate composition of crust and thin basal layer may represent a reworked terrain during the late-Archean.

Key words: Tomography; Composition of the continental crust; Cratons; Crustal structure; Asia.

1 INTRODUCTION

Knowledge of the composition of crust and its thickness is critical to understand the origin and evolution of the continent. While, the upper crust is better understood through surface geochemical analysis, our knowledge of the middle and lower crust remains poorly constrained. For example, it is argued that seismic wave velocity in the lower crust could vary significantly (V_p ∼ 6.5–7.1 km s^{-1}), and may be suggestive of very distinct lithologies and hence the process of evolution. In a recent study, Hacker *et al.* (2011) argue for a more felsic and almost three times more radiogenic lower crust than that estimated earlier (Rudnick & Gao 2003). This has implication for the understanding of the thermal state of lithosphere and emphasizes the need for an accurate description of the thickness and the seismic wave velocity of individual segments of the crust.

One of the primary issues remains to be resolved in understanding the evolution of continental crust is how an andesitic to dacitic crust has formed, when most of the mantle-derived magma is basaltic in nature (Hawkesworth & Kemp 2006; Hacker *et al.* 2011). This requires mapping the compositional similarity or diversity of crust at varying depth and geological time. Equally important is defining the nature of Moho, conventionally defined as a first-order compositional discontinuity, where seismic wave velocity increases sharply from normal felsic–mafic crust ($V_p < 7.0$ km s^{-1}, $V_s < 4.0$ km s^{-1}) to a typical mantle value with $V_p > 7.8$ km s^{-1} and $V_s > 4.3$ km s^{-1} representing ultramafic peridotites (White *et al.* 1992; Christensen & Mooney 1995). This scenario suggests a thin 1- to 2-km-wide transition at the Moho (Collins 1991; Korenaga & Kelemen 1997). Griffin & O'Reilly (1987) and Mengel & Kern (1992) argue that the Moho does not necessarily correspond to the crust–mantle

boundary. From a global study of crustal scale wide angle profiles, Mjelde *et al.* (2013) observe that Moho in selected areas may represent the top of lower crustal eclogites related to past orogenies (Olafsson *et al.* 1992). Transformation of mafic rocks (pyroxene–garnet granulite facies) to eclogite occurs at the base of originally thickened crust at a depth of about 50–70 km. Finally, due to combined effect of isostatic relaxation and erosion, the original root is transported to a depth of 30–50 km. Such well-preserved crustal roots reaching locally to 60 km have been mapped in cratonic regions of Europe (Artemieva & Meissner 2012). Due to similar seismic wave velocities of eclogite and peridotite, it is not easy to make distinction between them and require additional constraints like mapping of anisotropy and density (Worthington *et al.* 2013). A lower crust eclogite usually has density of 3.5 g cc^{-1} whereas partly eclogitic lower crust could have density similar to the underplated material (about 3.0 g cc^{-1}). Besides crustal composition, we also investigate here nature of the Moho topography, that is, is Moho flat or can have rugged topography? In either case it is enigmatic, for example, we have inadequate knowledge of the process responsible for generation of a nearly flat Moho or how block of very distinct Moho depth adjacent to each other survived through time (Kusznir & Matthews 1988; McBride 1995; Diaconescu *et al.* 1998; McKenzie *et al.* 2000).

Understanding the physico-chemical property of the crust and the nature of crust–mantle boundary is therefore important to model the processes responsible for making of the continental crust, its correlation with surface geology and the survival of the crust through billions of years. To answer some of the above issues, we present here shear wave velocity of the crust in the Dharwar Craton, using joint inversion of telseismic receiver functions from 50 broad-band seismographs, evenly sampling the region, with the Rayleigh-wave group velocity data (5–70 s). The dispersion data in the period 5–28 s are generated using ambient noise, and additional measurement in 40–70 s periods are taken from Acton *et al.* (2010).

2 GEOLOGY AND CRUSTAL STRUCTURE

The Dharwar Craton in the southern part of India is an Archean continental fragment with a continuously exposed crustal section from low-grade gneisses and greenstone basins in north to granulites in the south (Fig. 1). Based on the ages and the lithologies, the craton is divided into the Western Dharwar Craton (WDC) and Eastern Dharwar Craton (EDC) with Chitradurga Schist Belt (CSB) as the boundary (Naqvi & Rogers 1996). The WDC is made of 3.36–3.0 Ga gneisses and greenstone with 2.5 Ga granite. The oldest rocks are largely undeformed tonalitic gneisses in the south-central part of the WDC. Rb–Sr and Pb–Pb isochrons suggest age of about 3.36 Gyr for the greenstone belts in southern block of the Dharwar Craton, generally referred as 'Sargur Group' (red ellipse in Fig. 1), while the northern part constitutes the 2.6 Ga Dharwar Basin (black ellipse in Fig. 1) primarily composed of metasedimentary and metavolcanic rocks that lie over the gneisses. The central region of the WDC contains the basal metavolcanics of about 3.0 Ga (Drury *et al.* 1984). The WDC shows an increasing degree of metamorphism and exposes rocks from ∼3 kbar and 500 °C (greenschist facies) in central part (at 15°N**)** to ∼8–9 kbar and 800 °C (granulite facies) at 13°N in south corresponding to tectonic upliftment and erosion of ∼9 and ∼25 km, respectively. The WDC in the north is covered by the Proterozoic Kaladgi Basin (KB) and Bhima Basin (BB) and the Deccan Volcanic Province (DVP).

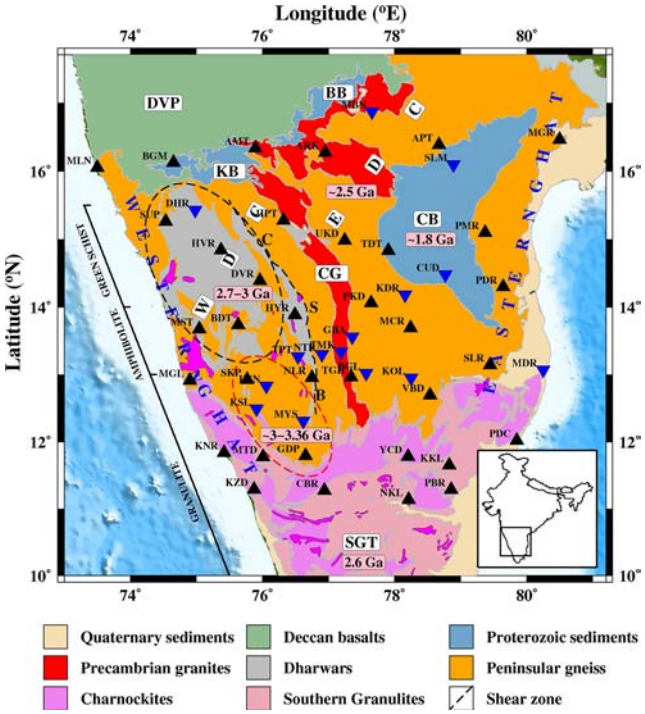

Figure 1. Tectonic map of south India shield showing major geological terrains with ages, tectonic features. EDC, East Dharwar Craton; WDC, West Dharwar Craton; SGT, Southern Granulite Terrain; DVP, Deccan Volcanic Province; CB, Cuddapah Basin; CG, Closepet Granite; CSB, Chitradurga Schist Belt; KB, Kaladgi Basin; BB, Bhima Basin. Dharwar schist (north) and greenstone belts (south) of the WDC are marked by black and red dashed ellipses, respectively. The seismic stations used in the study are shown as black triangles (2009–2011) and blue inverted triangles (1998–2002).

The EDC is dominated by the late Archean (∼2.7 Ga) calc–alkaline complex of juvenile and anatectic granites, granodiorites and diorites (Drury *et al.* 1984; Bouhallier *et al.* 1995; Chadwick *et al.* 2000) and is also termed as the Dharwar batholiths with granodioritic composition. The EDC is in thrusted, contact with the Proterozoic Cuddapah Basin (CB) and the Eastern Ghat Granulite terrain (Eastern Ghat). The CB is a prominent geological feature containing numerous mineral deposits. The basin, which largely evolved around 1700 Ma, is block faulted. Its southern part is affected by several episodes of igneous activity (Nagaraja Rao *et al.* 1987). Sediments in the southern part are more metamorphosed compared to the sediments in the north. The easternmost geological terrain is the Eastern Ghat characterized by positive Bouguer anomaly (Kaila & Bhatia 1981). It is inferred to be in thrust contact with the CB. All rocks within the Eastern Ghat are either igneous or metamorphosed sediments (dominantly Khondalite and pyroxene-free rocks). These rocks are dated from 1615 to 995 Ma. The westernmost geological block of the study region is the Western Ghat, an ∼50-km-wide coast parallel topographically high (∼1.2 km) belt that is linked to the separation of Madagascar from India at ∼90 Ma (Storey 1995). The craton progressively transitions into Archean metamorphic terrain (2.6 Ga) widely known as the Southern Granulite Terrain (SGT).

Our present understanding of the nature of the crust beneath the Dharwar Craton is largely based on the seismic wave velocity derived from the modelling of wide angle reflection and refraction measurements along a profile; surface wave and receiver function modelling from a few broad-band seismograph locations. Seismic reflection/refraction data across the central part of WDC/EDC

suggest that the crust is broken into blocks with distinct Moho depths varying from 34 km in the east to 41 km in its west (Kaila *et al.* 1979; Roy Chaudhary & Hargraves 1981). Kaila & Krishna (1992) re-analyze these data and model an upper crust with *P*-wave velocity of 6.4 km s^{-1}, lower crust velocity 6.7 km s^{-1}. Krishna & Ramesh (2000) invert the seismic wave field from mine tremors and explosions recorded on the Gauribidanur (GBA) short period seismic array in the EDC. They find the Moho depth beneath GBA to be 34–36 km and the *Pn* velocity to be 8.2 km s^{-1}. Inversion of Rayleigh-wave phase velocity in the EDC suggests an average crustal thickness of 35 km which consists of layer with $V_s \sim 3.66$ km s^{-1}, and thickness ∼12 km overlying a 3.81 km s^{-1} and 23-km-thick lower crust (Mitra *et al.* 2006). Receiver function modelling studies from a few broad-band seismographs (Gaur & Priestley 1996; Gupta *et al.* 2003a,b; Rai *et al.* 2003; Sarkar *et al.* 2003; Jagadeesh & Rai 2008; Julià *et al.* 2009) suggest a felsic and transparent crust with average $V_s \sim 3.7$ km s^{-1} beneath the EDC in contrast with a layered crust with mafic component ($V_s \geq 4.0$ km s^{-1}) in the lowermost part of the crust beneath the WDC. Also, the EDC is characterized by a nearly flat Moho at ∼35–38 km, while the WDC, despite being older, has a Moho depth varying in steps from 42 to 55 km. The thickest crust (∼55 km) is observed beneath the oldest geological (3.36 Ga) sequence of greenstone belt. Rayleigh-wave group velocity measurements from earthquake sources recorded at limited observation locations have been used to generate 3-D tomographic *S*-velocity image of the region (Mitra *et al.* 2006; Acton *et al.* 2010). However, due to poor lateral resolution (5° × 5°) and poor depth control in shallow crust (period >12 s) these studies can at best be used to model the regional velocity structures. Kiselev *et al.* (2008) jointly inverted the *P* and *S* receiver functions and teleseismic *P*- and *S*-wave traveltime residuals at 10 seismograph stations in the Dharwar Craton. They also observe similar differences in crustal structures between the EDC and the WDC as discussed earlier. Due to inadequate number of broad-band seismographs in the region, it has not been possible to investigate terrain wise velocity structure. This research contribution presents a detailed study over the Dharwar Craton using a well-distributed network of instruments and provides a better constrained velocity model that reveals the crustal scale complexity linked to the evolution of the craton.

3 DATA ANALYSIS

To study the seismic velocity structure beneath the Dharwar Craton, we apply twofold approaches: computation of Rayleigh-wave dispersion tomography from ambient noise and jointly invert it with the receiver function measurements. We perform ambient noise tomography using waveforms recorded on 35 broad-band stations during 2009 February to 2010 August (Fig. 1). The interstation distance varies from 55 to 820 km. These waveforms are recorded at 50 Hz sampling frequency by seismographs that include REFTEK 130 data acquisition system and Guralp make CMG 3T/3ESP broad-band sensors. The stations are uniformly distributed over the region providing good ray path coverage for the study. We perform cross-correlation of ambient noise data and extract Rayleigh-wave group velocities between all station pairs at periods from 5 to 28 s. These are then used to generate 2-D tomographic image of the group velocity at different periods using block parametrization of size 0.5° × 0.5°. We supplement these measurements in each of the block with group velocity data at longer period (40–70 s) from an earlier study using earthquake sources (Acton *et al.* 2010).

We create the 3-D shear velocity image of the crust beneath the Dharwar Craton from the 1-D velocity–depth model obtained beneath individual station. The station-specific velocity model is computed through joint inversion of receiver function and dispersion data. Receiver functions are computed from 50 stations, of which 35 stations are operated during 2009–2010 as mentioned above; the other 15 are from an earlier experiment during 1998–2002 (Gupta *et al.* 2003a,b). Details of the station information are presented in Table S1.

4 AMBIENT NOISE TOMOGRAPHY

Traditionally, surface wave tomography using earthquake waveform has been successfully used in reconstruction of regional velocity images. However, the approach suffers from two primary weaknesses: lack of uniform illumination of velocity images generated due to its dependence on earthquake source location, and loss of high-frequency information (<20 s period) because of intrinsic attenuation and scattering which leads to poor resolution of the shallow crustal structure. These problems can be overcome using ambient noise (Ritzwoller 2009) as the approach is independent of the seismic sources. The ambient noise tomography has been extensively applied over varied geological terrains (Shapiro *et al.* 2005; Yao *et al.* 2006; Lin *et al.* 2007; Yang *et al.* 2007, 2008; Bensen *et al.* 2008; Liang & Langston 2008; Pawlak *et al.* 2011).

4.1 Green's function computation

Theoretical works (Weaver & Lobkis 2001; Derode *et al.* 2003; Snieder 2004; Wapennaar 2004; Larose *et al.* 2005) demonstrate that if the sources of the ambient noise are evenly distributed and recorded by sensors at two points $A(\varphi_A)$, $B(\varphi_B)$, then time derivative of the correlation is the exact Green's function of the medium, as if the source is at either *A* or *B*:

$$\delta_\tau C_{AB}(\tau) = \delta_\tau \int \varphi_A(t)\varphi_B(t+\tau)\,dt \qquad (1)$$

$$\propto G^+(A, B, \tau) - G^-(A, B, -\tau),$$

where G^+ and G^- are the causal and anticausal Green's function. Snieder (2004) shows that only the sources near the line connecting two stations contribute to the signals observed in the cross-correlation function. Sources at opposite side of the line will contribute to the signal at positive lag (causal) and negative lag (acausal) in the cross-correlation function, respectively.

To compute the Green's function from the vertical component of the ground velocity record, we carry out pre-processing of waveform recorded at individual station following Bensen *et al.* (2007). These include: resampling of the data to 1 Hz, removal of the instrument response, bandpass filtering the seismograms in the frequency range 4–50 s, time domain normalization and spectral whitening. In time domain normalization we use an event detection and signal removal technique. In this approach the data are first divided into hour blocks and blocks containing signals above a threshold are discarded. The selection of the threshold is arbitrary. Setting threshold too high provides no normalization while setting it too low discards too much data. An appropriate choice is found to be about 10 times the absolute mean. Spectral whitening is used after normalization, which reduces the natural imbalances in ambient noise spectrum and broadens the ambient noise signal in cross-correlation. Cross-correlation is performed hourly and then stacked to increase the signal-to-noise ratio (SNR). Sabra *et al.* (2005) show that the SNR

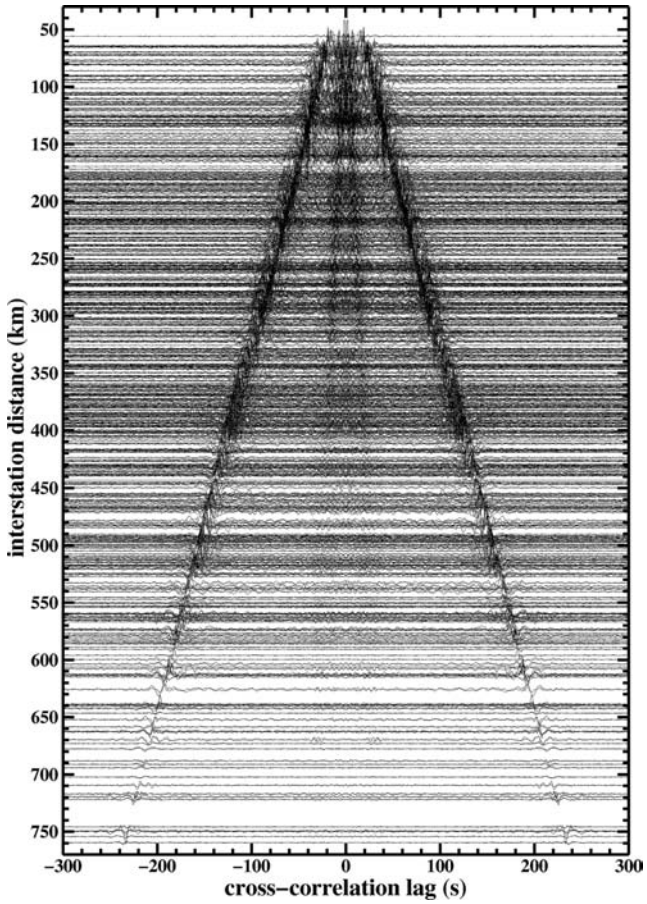

Figure 2. Record section of cross-correlation showing both positive and negative correlation lag time. Data set is filtered in the bandwidth 5–50 s.

of the Green's function is proportional to the square root of the recording time.

Depending on the group velocity of the waves and the longest interstation distances, we store our cross-correlation from −300 to 300 s which is then converted into one-sided signal (symmetric signal) by averaging the causal and acausal part. Fig. 2 shows an example of 18-month stacks of cross-correlation plotted as a record section. Clear signals are observed for both the positive and negative correlation lag time.

4.2 Dispersion analysis

The next step in the analysis is the computation of group velocity dispersion from the Green's function. For each Green's function computed, we select a time window centred on the fundamental mode Rayleigh wave. These windows are filtered using a set of narrow frequency bands. We show a metric broad-band cross-correlation subjected to a series of narrow bandpass filters centred in the frequency bands 5–10, 10–15, 15–20, 20–25 and 25–30 s (Fig. 3). The group velocity dispersion curve for this period and amplitude for each stacked Rayleigh-wave Green's function is estimated by using multiple-filter technique (MFT; Dziewonski *et al.* 1969; Herrmann 1973). Using this approach, we construct energy–period diagram of the surface wave part of the seismogram which matches the maximum energy part of the fundamental mode Rayleigh-wave part. The trend of the maximum energy forms a dispersion ridge. Fig. 4 shows an example of time frequency plot and the dispersion graph for the correlation data corresponding to station pair MST–PKD

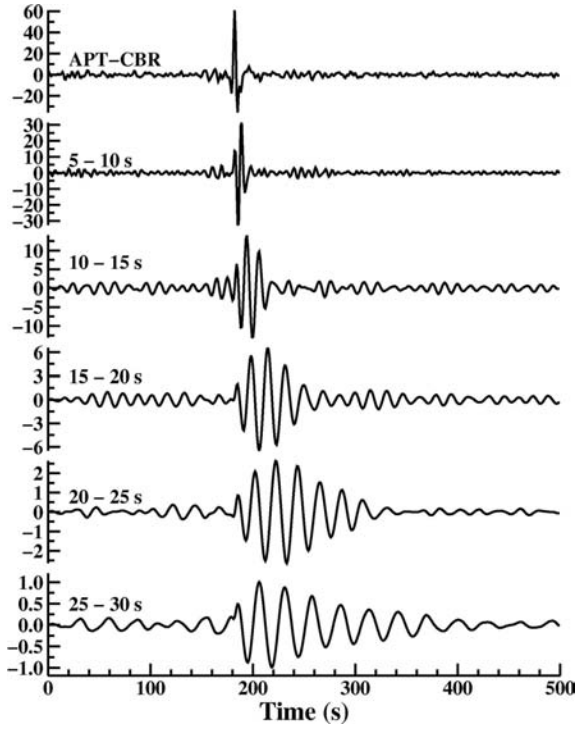

Figure 3. Symmetric bandpass cross-correlation data, for 18 months, from station pair APT–CBR filtered in the frequency band 5–10, 10–15, 15–20, 20–25 and 25–30 s.

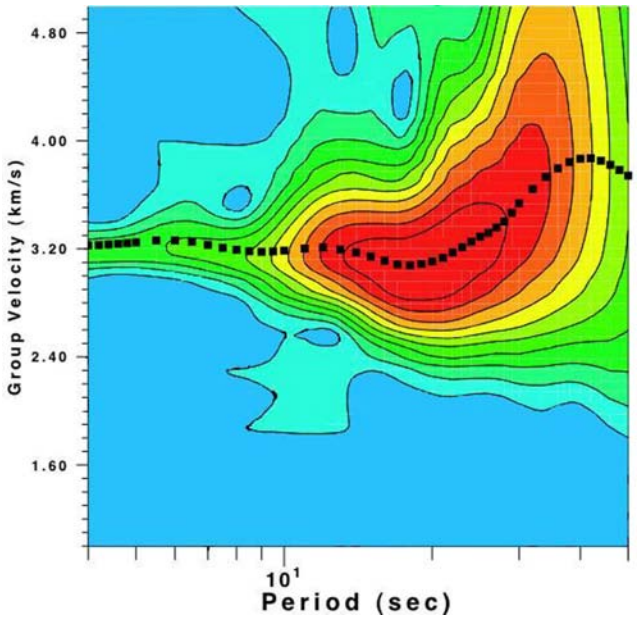

Figure 4. Frequency–time image of the symmetric component of the trace from station pair MST–PKD.

(location shown in Fig. 1). For further analysis, we select group velocity measurements having SNR $\geq$ 5 and interstation distance more than three times the wavelength at the considered period. SNR is defined as the ratio of peak amplitude in the signal window to rms noise in the trailing noise window (Bensen *et al.* 2007). Ray path coverage in the region at different time periods is shown in Fig. 5.

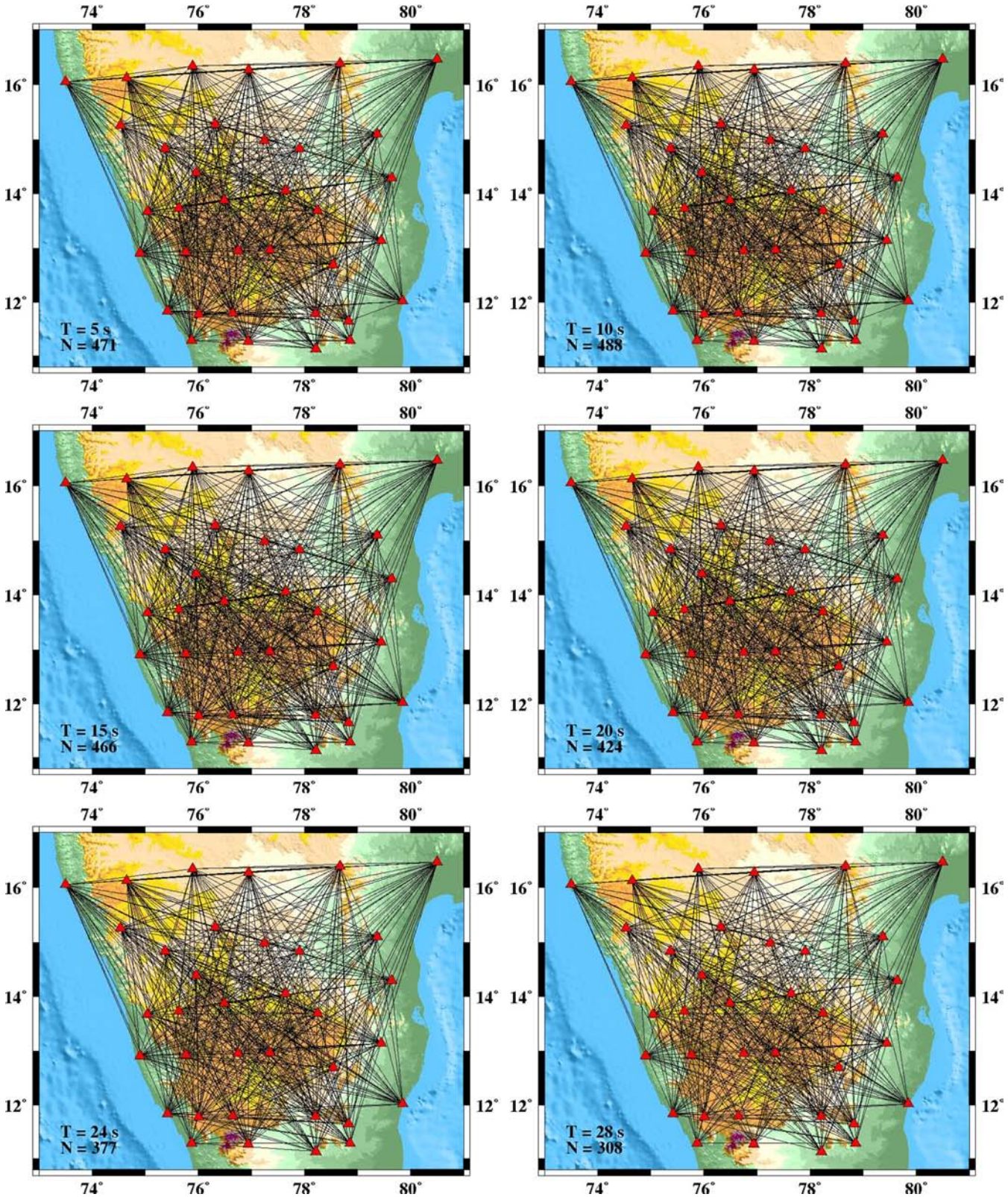

Figure 5. Ray path coverage in the Dharwar Craton at different periods (5, 10, 15, 20, 24 and 28 s). Number of ray paths (*N*) is plotted at the bottom left corner of each plot.

4.3 Group velocity maps

The group velocity inversion at each period has been performed from a set of two point Rayleigh-wave dispersion measurements using Fast Marching Surface Tomography (FMST) computer code by Nick Rawlinson at the Australian National University, Australia. The method combines the Fast Marching Method (FMM; Rawlinson & Sambridge 2004a,b) for calculation of forward problem and

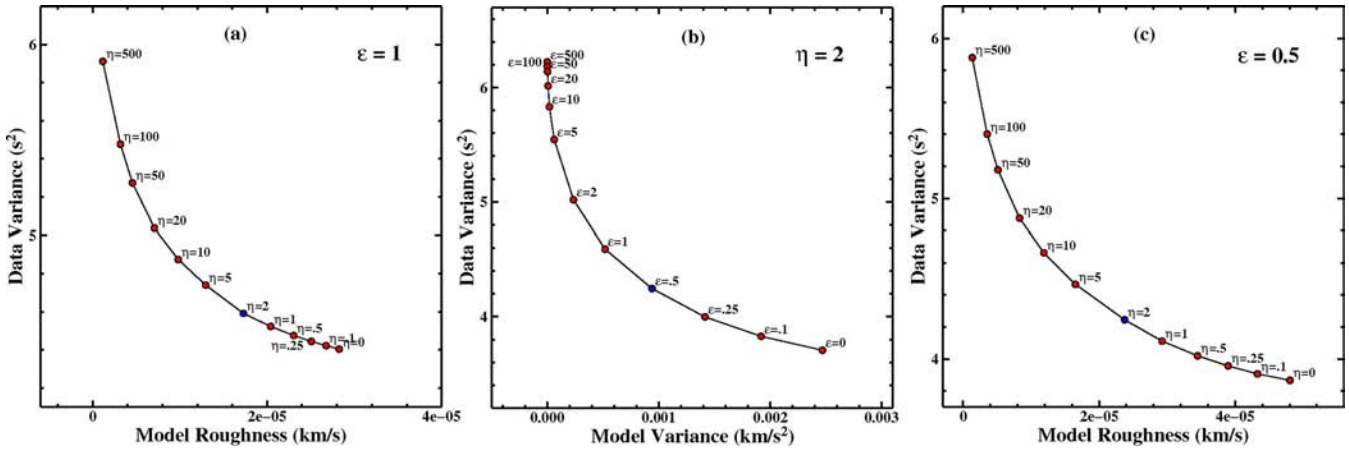

Figure 6. Estimation of optimum damping and smoothing parameters. (a) Varying smoothing parameter (η, red dots) keeping damping parameter (ϵ) fixed at 1. $\eta = 2$ (blue dot) is chosen from the curve. (b) Varying ϵ keeping smoothing parameter fixed at $\eta = 2$. The value $\epsilon = 0.5$ (blue dot) is chosen as optimum. (c) Varying η keeping $\epsilon = 0.5$ fixed. The value $\eta = 2$ still appears to be a good choice.

subspace method (Kennett *et al.* 1988) for inversion. A detail of the methodology is given by Rawlinson & Sambridge (2004a) and Saygin & Kennett (2012).

We evaluate spatial resolution of the surface wave tomograms using checkerboard test considering square cells of side 0.5° with velocity perturbations of ±8 per cent relative to an average background velocity for the given time period. To test the stability and tolerance of velocity images, we compute synthetic traveltimes by adding a Gaussian noise with standard deviation of average traveltime uncertainties in real data at each period (Mottaghi *et al.* 2013). The noise-added traveltimes are inverted at each period to generate the group velocity tomograms. For reconstructing the velocity image, we use an optimal value of damping (ϵ) and smoothing (η) parameters obtained by studying the trade-off between the data and the model variance for different values of the two parameters. First, we hold damping parameter fix ($\epsilon = 1$) and vary η (Fig. 6a). The graph suggests $\eta = 2$ as the optimal value. For this value of η, ϵ is varied to study the trade-off between model and data variance (Fig. 6b). This study suggests damping parameter $\epsilon = 0.5$ to be the optimal. We recompute the η with $\epsilon = 0.5$. The resulting trade-off curve (Fig. 6c) shows that $\eta = 2$ is still a good choice of smoothing parameter. The checkerboard input velocity model and the corresponding recoveries for 5 and 28 s periods are shown in Fig. 7. For the remaining periods, velocity recoveries are shown in Fig. S1. Due to uniform distribution of stations, the images are well resolved for most parts of the region over all the time periods from 5 to 28 s. For better quantification of the resolution of the reconstructed image in a cell i, we define a resolvability variable $R_i = 0.5(v_{i+}v_i')^2/[(v_i)^2+(v_i')^2]$ (Zelt 1998), where v_i and v_i' are the true and recovered velocity models. For a perfectly resolved cell $R = 1$. The R value decreases with increasing difference between recovered and theoretical models. Resolvability for individual cells at 5 and 28 s periods (thick red line in Fig. 7) show that 75 per cent of cells have $R = 0.9$.

4.4 Group velocity variation and surface geology

The absolute Rayleigh-wave group velocity maps are presented at periods 5–28 s (Fig. 8). To assess the reliability of computed group velocity using noise data, the result is compared with two different sets of observations: (1) the group velocity results from earthquake source and (2) the group velocity results at 15, 20, 25 and 30 s periods from global surface wave studies (Pasyanos 2005). Group velocity dispersion values are evaluated for two earthquake (red stars in Fig. 9a) waveforms recorded by the stations YCD and KKL. Two vertical component waveforms recorded by the station KKL are shown in Fig. 9(b). The average group velocities are also calculated between 5 and 28 s from ambient noise tomography results by averaging the group velocity data in 0.5° bin along the earthquake path. These results (Fig. 9c) show very similar behaviour within the limit of averaging. Variation at 15 s from global measurements could be due to averaging, which is much larger for global data.

Sensitivity kernels of Rayleigh-wave group velocities corresponding to a velocity model (Fig. 10a) are plotted in Fig. 10(b). Rayleigh waves at 5 s period are primarily sensitive to shallow crust structure in the depth of 4–10 km; the 10 s image represents the top 5–15 km, 20 s image represents the velocity structure in the depth 10–30 km, while at 28 s the group velocity image is sensitive to structure in the depth 20–35 km. With increasing period of the group velocity, the sensitivity kernel gets more flat indicative of larger depth averaging.

At 5 s period, the tomographic image (Fig. 8) is likely to be well correlated with the surface geology. In the WDC, we observe lower velocity (∼3.15–3.25 km s^{-1}) in the north coinciding with the Dharwar Basin and progressively increasing (∼3.25–3.40 km s^{-1}) towards the south, further into the contiguous SGT. These high-velocity zones correlate with the ultramafic greenstone belt in the south WDC and the exposed mid-lower-crust domain. In the EDC and CB, there could be lateral smearing of velocity due to proximity of the two terrains. In the CB the velocity increases progressively from 3.15 km s^{-1} in north to 3.30 km s^{-1} in its southern part. This is expected, as the sedimentation in the north CB is at ∼800 Ma as compared to ∼1.5–1.7 Ga in south. Between east and west Dharwar, the Closepet Granite (CG) shows N–S segmentation: northern part with a number of shear zones and schist belts has higher velocity (3.30–3.40 km s^{-1}) compared to the southern part. Broadly speaking, high-velocity zones are correlated with schist belts representing metavolcanics in the Dharwar Craton, exhumed granulites of the WDC and SGT, while lower velocity regions are the locations of late Proterozoic sediments in CB or Archean sediments in the Dharwar. In the near surface the two Archean blocks, the WDC and the EDC, are well separated. The western boundary of N–S trending 3.3 km s^{-1} velocity contour is well correlated with the CSB,

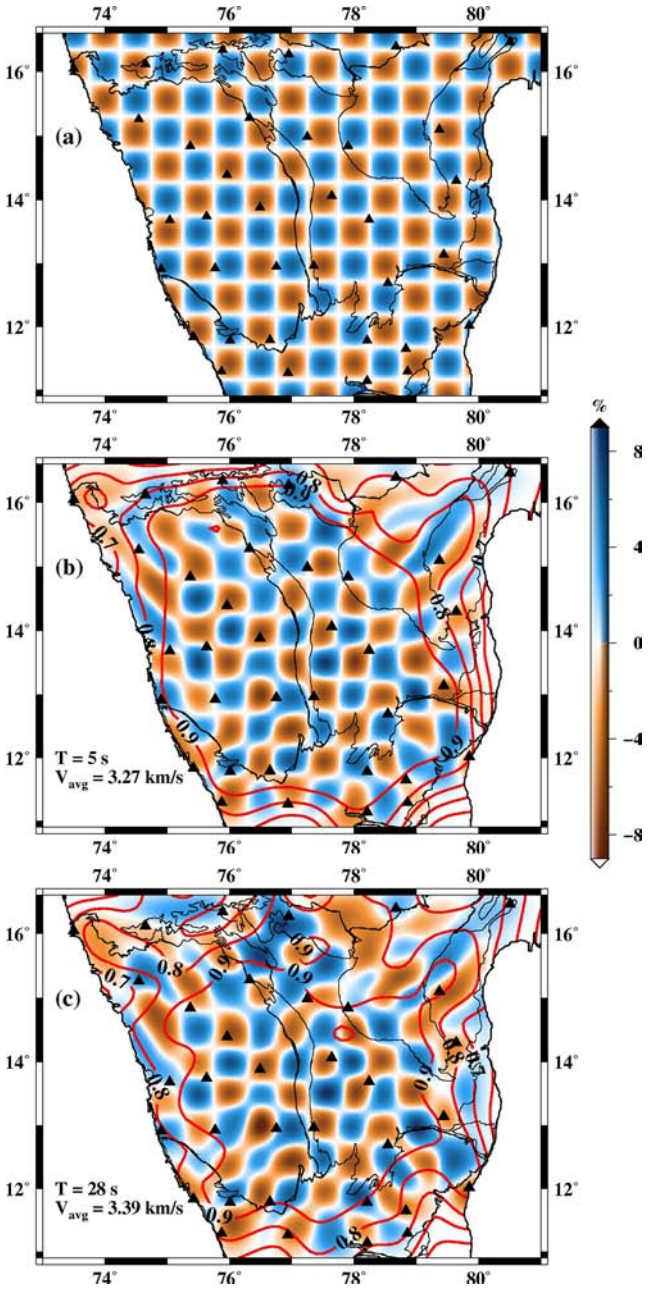

Figure 7. Checkerboard input velocity model (a) and recoveries for group velocities at two periods, 5 s (b) and 28 s (c). Anomalies are plotted with respect to the average group velocity (bottom left corner) at that period. Red thick curves denote the contour of resolvability.

geologically defined as the boundary fault between WDC and EDC. This is marked as tectonic boundary in Fig. 8. Most of the higher and lower velocity patterns observed at 5 s period continue to occur at 10 s period (corresponding depth of 5–15 km) group velocity image also, though with reduced velocity. Group velocities at 15 and 20 s are mostly sensing 10–25 km depth. At these depths ranges, high group velocity is observed (3.2–3.3 km s^{-1}) in the southern part of the WDC.

The group velocity maps at 24 and 28 s are primarily sensitive to velocity structure at depth varying from 18 to 30 km. At these depth ranges, the EDC and the WDC show similar group velocity of ∼3.22–3.26 and 3.38–3.40 km s^{-1}. The observed velocity variations for longer periods (>20 s) are laterally less pronounced than those of the shorter periods, which may be due to the more homogeneous crust at these depths. These velocity maps provide a qualitative estimate of the variability of group velocity at different time periods (hence depths).

5 RECEIVER FUNCTION

Receiver function is a well-known technique to find the crust and upper-mantle velocity structure (Langston 1977; Ammon *et al.* 1990; Ammon 1991) using *P*-to-*S* converted teleseismic waves at discontinuities underneath a three-component seismic receiver. For receiver function calculation, we use earthquakes of magnitude more than 5.5 and epicentre distance between 30° and 95°. This epicentre distance range avoids multiple arrivals in the direct *P* wave occurring at distances less than 30° caused due to triplication and also complication at distances greater than 95° resulting from core–mantle boundary. We visually check seismograms corresponding to these events and only those with clean *P* arrival are used for receiver function calculation. We cut the data trace of seismic events to a length of 150 s (30 s pre-event and 120 s post-event) and filter using Butterworth high-pass filter with a corner frequency of 0.02 Hz. After removing the mean and trend of the data, horizontal components (North/South and East/West) are transformed into radial and transverse components, respectively. These components are deconvolved in time domain using iterative deconvolution approach (Ligorría & Ammon 1999). In each iteration, receiver function approximation is improved by adding a peak, convolving this with vertical component and then compares the result with the radial component. The process is iterated 200 times to compute the receiver function. In receiver function computation, a low-pass Gaussian filter (Gw) is commonly used to clean high-frequency noise and is defined as

$$G(\omega) = \exp(-\omega^2/4a^2), \quad (2)$$

where a is Gaussian width, which controls the frequency (ω). For example, Gw1.6 and Gw2.5 correspond to 0.8 and 1.2 Hz low-pass filter, respectively, to a seismogram. As a rule of thumb, corresponding to Gaussian width, a, frequency is approximately equal to $a/2$. In our study, we use Gw1.6, because higher Gaussian width contains noisier receiver function, while lower Gaussian width, merge the intracrustal layers and make them flat. We select over 2500 receiver functions, with more than 80 per cent waveform recovery, from an initial nearly 4000 receiver functions. The percentage of recovery of the original radial waveform is evaluated from the rms misfit between the original radial waveform and the convolution of the radial receiver function with the original vertical component.

To enhance the amplitude of Moho-converted *P*-to-*S* conversion (*Ps*) and its multiples, events clustered in narrow epicentre distances and backazimuths are stacked to produce a single estimate of the receiver function. Since receiver functions in narrow backazimuth and epicentral distance bin look similar, no weight is assigned to any receiver function for stacking. One standard deviation ($\pm 1\sigma$) bounds are determined from the variance of the stacked data. These bounds are used to check the fit of receiver function in modelling. In this study, we use ±8° bounds for both epicentral distance and backazimuth. Depth resolution in 1-D receiver function inversion is approximately half the wavelength of the converted wave–a relationship determined empirically with both the synthetic data (Bostock & Rondenay 1999) and field data (Rychert *et al.* 2007). For average V_s of 3.5 km s^{-1}, the corresponding wavelength is 4.3 km leading to resolvable layer thickness of ∼2 km.

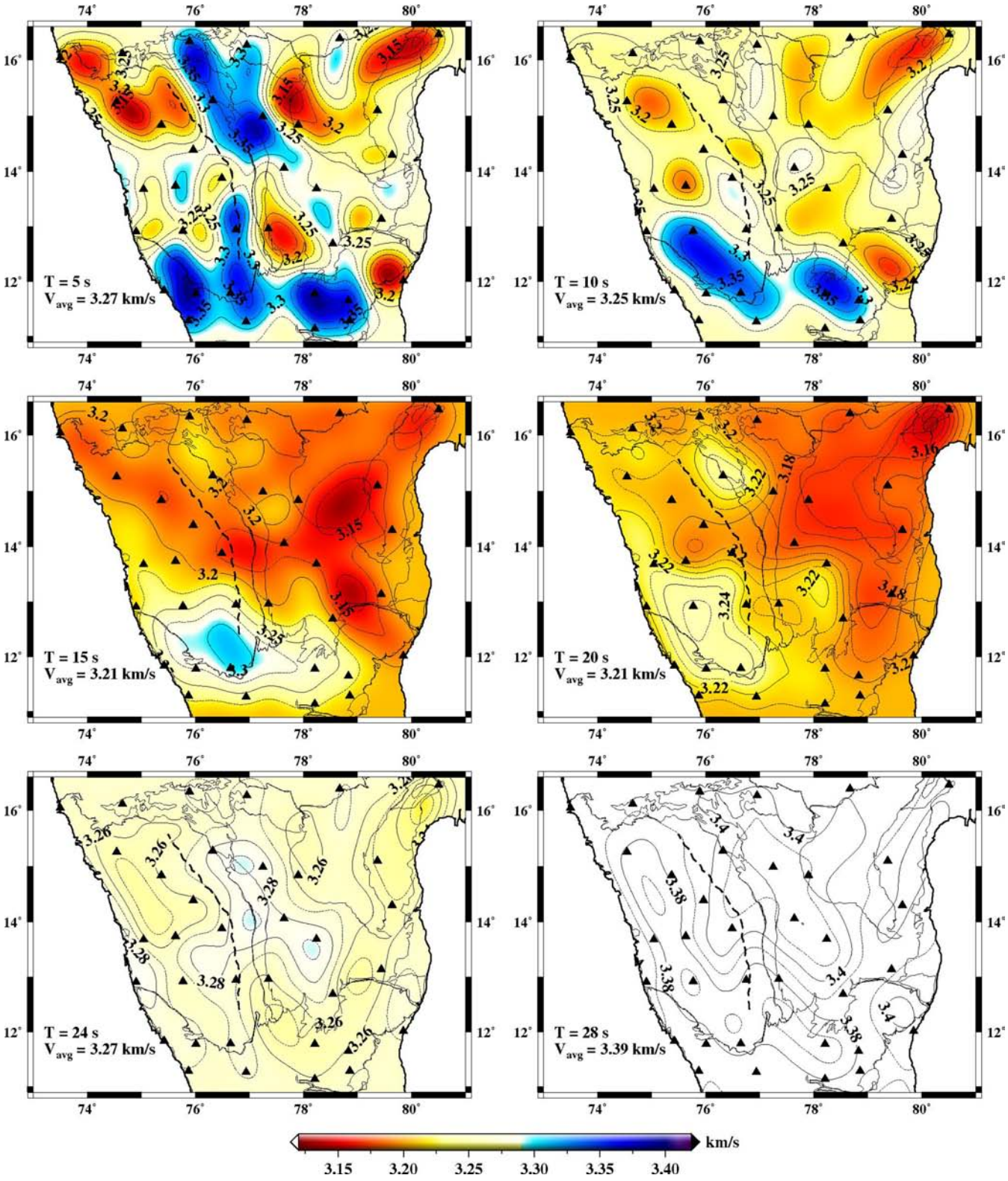

Figure 8. Group velocity maps for selected periods of 5, 10, 15, 20, 24 and 28 s. Group velocity variations are with respect to the average group velocity (bottom left corner) at that period. At 28 s only group velocity contours are plotted.

6 JOINT INVERSION OF RECEIVER FUNCTION AND SURFACE WAVE DATA

Shear velocity structure beneath each of the stations of the Dharwar Craton has been modelled using the joint inversion of receiver function and surface wave dispersion data. While receiver function measurement is sensitive to impedance contrast across the layer, the surface wave data provide absolute value of the shear velocity in these layers. Further, due to higher frequency content, the receiver function has better resolution in depth as compared to

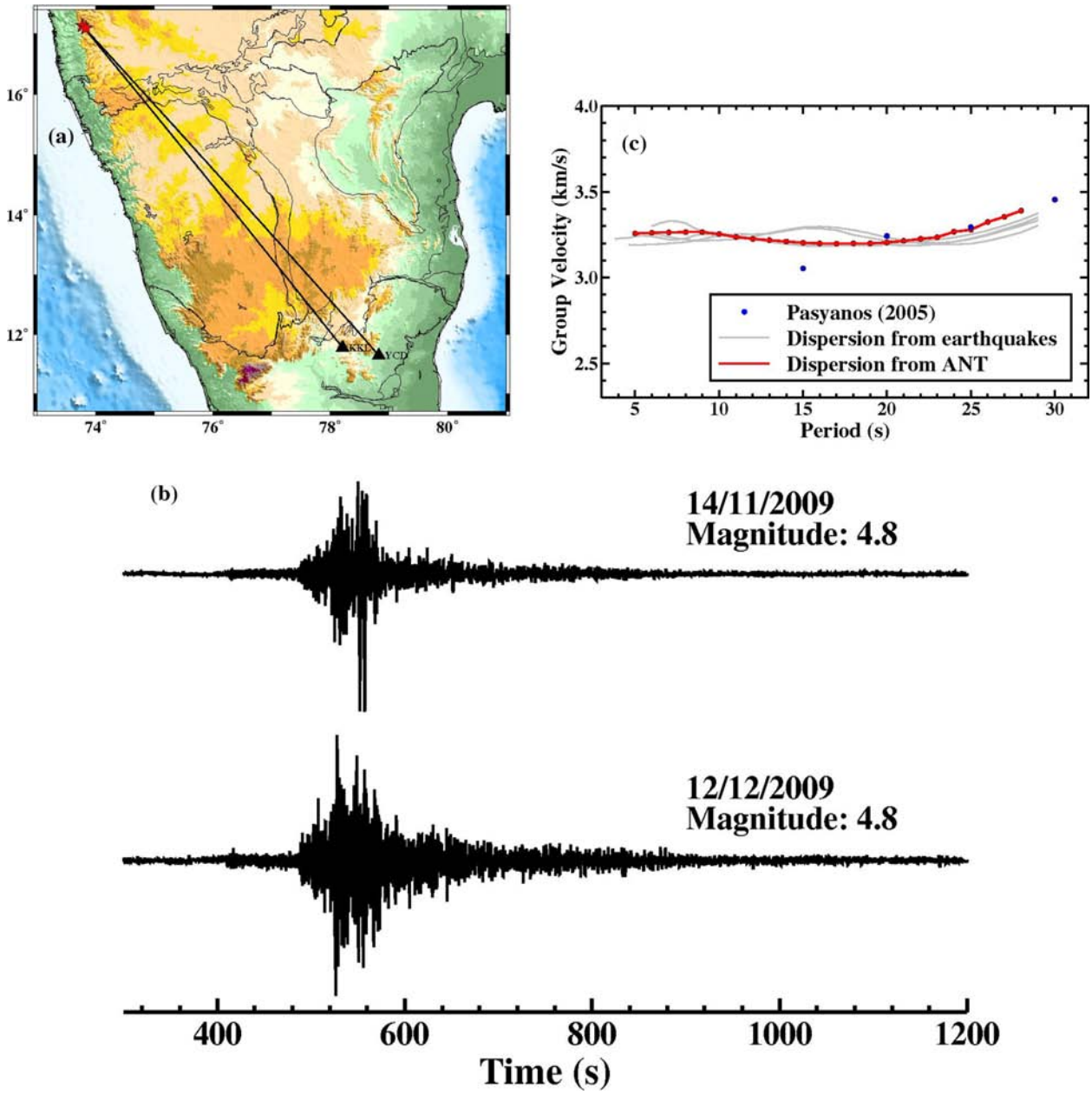

Figure 9. (a) Earthquakes (red stars) of magnitude 4.8 recorded by KKL and YCD stations. (b) Vertical waveforms of two earthquakes (Fig. 9a) recorded by KKL station. (c) Comparison of group velocity dispersion from earthquake data (grey curve), ambient noise tomography (red curve) and global surface wave study of Pasyanos (2005) (blue circle).

surface wave. Complementary nature of the two data sets are exploited through their joint inversion to produce better constrained velocity image. The joint inversion is performed following iterative linearized damped least-square technique of Julià *et al.* (2000). Here, we attempt to find an earth model that minimizes the functional S, defined as:

$$S = \frac{1-p}{N_r}\sum_{i=0}^{N_r}\left(\frac{O_{ri}-P_{ri}}{\sigma_{ri}}\right)^2 + \frac{p}{N_s}\sum_{j=0}^{N_s}\left(\frac{O_{sj}-P_{sj}}{\sigma_{sj}}\right)^2, \qquad (3)$$

where N_r and N_s are the total number of receiver functions and the surface wave data point, respectively; O_{ri} and P_{ri} are the observed and predicted receiver function at time t_i; O_{sj} and P_{sj} are the j-th observed and predicted surface wave dispersion; and σ_{ri} and σ_{rj} are the standard errors in each data set. The factor 'p' is an *a priori* value, called influence parameter that changes the influence of either data set on the minimization procedure. The value of p lies between 0 and 1. Fig. 11(a) shows the effect of varying p parameter on the shear velocity model for the station AMT. Setting $p = 0$ or 1 results in a solution based only on receiver function or only the dispersion data, respectively. As expected for $p = 0$, dispersion data are not fitted (black line in Fig. 11b) but receiver function is well fitted (black line in Fig. 11c), while for $p = 1$ dispersion data are well fitted (cyan line in Fig. 11b) but receiver function is poorly fitted (cyan line in Fig. 11c). For other values of p (0.2–0.8), V_s models and the fit of dispersion data and receiver function are quite similar. We fixed p to 0.5, which offers equal priority between fitting the receiver functions and the dispersion curve. The initial velocity model for inversion has layer thickness of 2 km down to a depth of 50 km followed by 5-km-thick layers (between

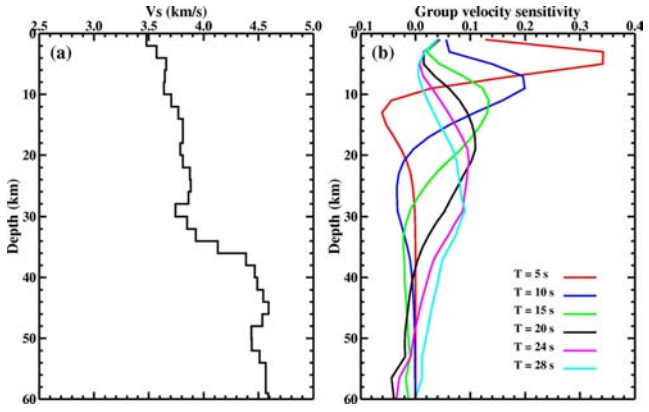

Figure 10. (a) Shear velocity model of AMT station. (b) Sensitivity kernels of fundamental mode Rayleigh-wave group velocities at 5, 10, 15, 20, 24 and 28 s periods corresponding to the shear velocity model (Fig. 10a).

50 and 200 km depth). Shear velocity of layers is considered as 4.5 km s^{-1} ($V_p/V_s = 1.73$ and density = 3.3 gm cm^{-3}). Convergence of the inversion models is generally achieved in 10 iterations. We, however, repeate the inversion procedure 20 times to get the final shear velocity model.

From ambient noise tomography, we compute group velocities for the periods 5–28 s, which have peak sensitivity down to 30–35 km depth (Fig. 10). For each station the dispersion data in a 1° circular bin, with station as centre, are averaged and $\pm 2\sigma$ error bounds are calculated. Using these data sets it is possible to estimate the crustal structure of the EDC stations, where crustal thickness is ∼35 km. For the stations of the WDC, SGT etc., where crustal thicknesses are more than 40–50 km, longer period group velocity data are needed for better resolution in depth. Rayleigh-wave group velocity data at longer periods (40–70 s) are taken from a tomographic study carried out by Acton *et al.* (2010) in the Indian shield. The combined group velocity dispersion data from 5 to 70 s are inverted jointly with the stacked receiver function estimated for each station using the joint inversion methodology of Julià *et al.* (2000) and Herrmann & Ammon (2004).

We discuss here the methodology to produce 1-D shear velocity model for station AMT. Fig. 12(a) shows the receiver functions plotted equispaced with increasing epicentral distance. Receiver functions in a backazimuth and epicentral bin (grey shaded area) are stacked. The stacked receiver function is jointly inverted with Rayleigh-wave dispersion data to estimate 1-D shear velocity structure beneath the station. Figs 12(b) and (c) show the fitted synthetic group velocity (red line), the observed group velocity (black and red dots) with error bounds (black bars) and the fitted synthetic receiver function (red line), stacked observed receiver function (blue line) with $\pm 1\sigma$ error bounds (grey shaded area), respectively, corresponding to the shear velocity model (red line) in Fig. 12(e). Christensen & Mooney (1995) and Christensen (1996) show that shear wave velocity in the lower crust cannot exceed 4.3 km s^{-1} and shear wave velocities above 4.3 km s^{-1} indicate the presence of lithology of mantle composition. Therefore, crustal thickness at each station is determined by placing Moho at the depth where shear wave velocity exceed 4.3 km s^{-1}. Moho (M) is marked by an arrow and the shaded portion denotes the basal layer with $V_s \geq 4.0$ km s^{-1} ($V_p > 7.0$ km s^{-1}). We also vary the Moho depth by ±2 km (Fig. 12e) and check that the synthetic receiver function lies within $\pm 1\sigma$ receiver function error bounds (Fig. 12d) to determine the bounds of the Moho depth.

Non-linearity and non-uniqueness are the two main problems in the receiver function inversion (Ammon *et al.* 1990). Non-uniqueness is significantly reduced by the joint inversion of the receiver function and surface wave dispersion data, and since two independent data sets are matched simultaneously limiting the likelihood of overinterpretation. Julià *et al.* (2000), using numerical experiment show that the starting half-space model characterized by

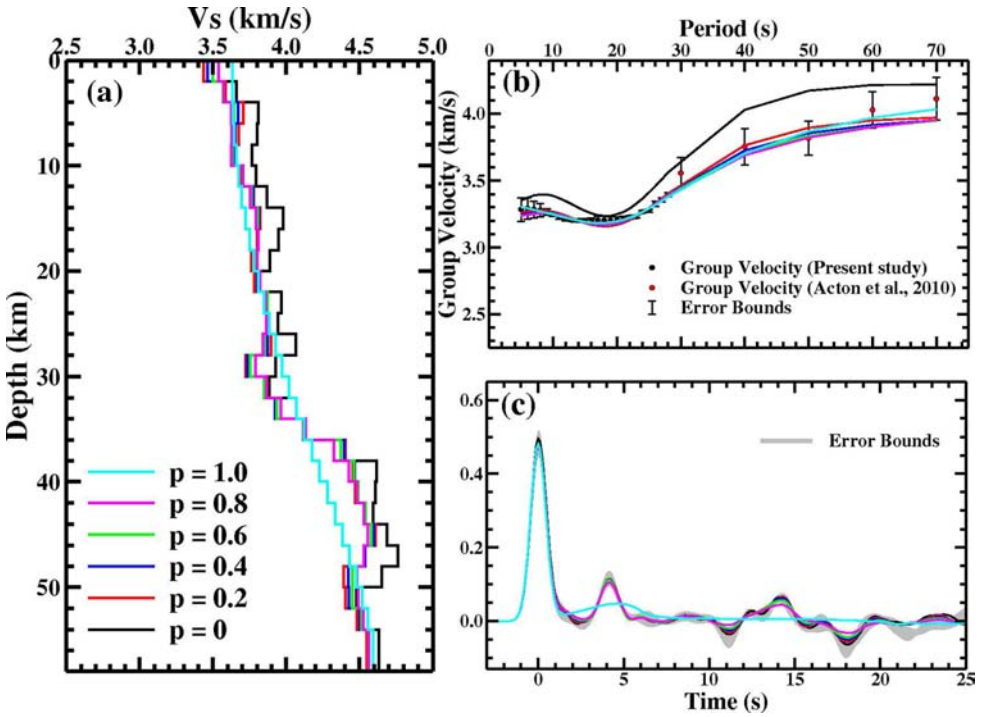

Figure 11. (a) Shear velocity models, (b) fitting of dispersion values and (c) fitting of receiver function for different values of p (influence parameter, see text for details).

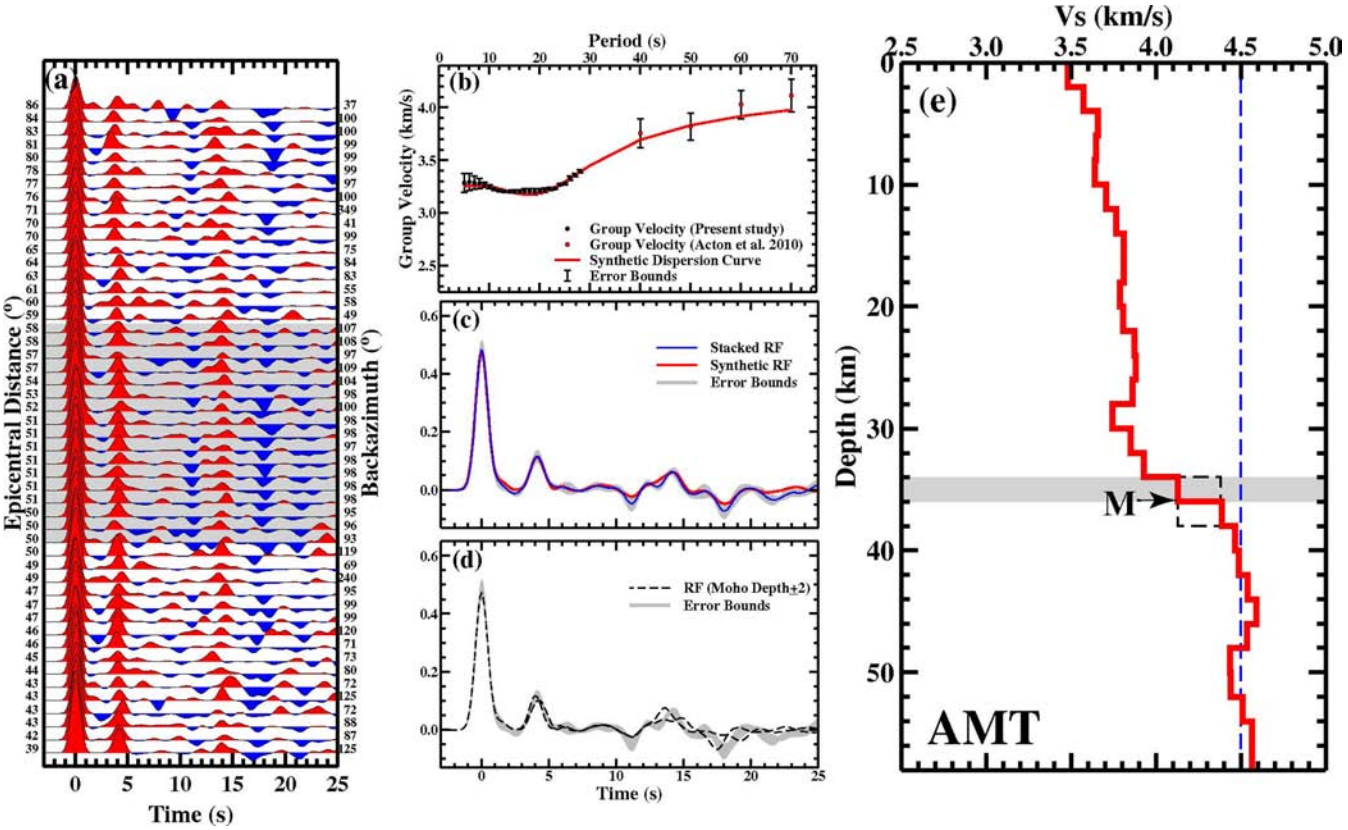

Figure 12. (a) Receiver functions for station AMT are plotted with increasing epicentral distance. Backazimuth values are also shown to the right of the plot. Receiver functions in the grey shaded zone are stacked and inverted jointly with group velocity dispersion data. (b) Fitting of synthetic dispersion curve (red line) with observed group velocities from ambient noise (black circles) and earthquake tomography (red circles) with error bars (black vertical bars). (c) Fitting of stacked receiver function (blue line) with synthetic receiver function (red line) and $\pm 1\sigma$ error bounds. (d) Synthetic receiver functions (dashed lines) corresponding to the Moho depth variation by ± 2 km (black dashed line in panel e). (e) Final shear velocity model (red line) corresponding to the half-space initial model with $V_s = 4.5\,\mathrm{km\,s^{-1}}$ (blue dashed line). M denotes the Moho discontinuity and grey shaded region denotes the thickness of the basal layer.

some realistic velocity is enough to make iterative process in joint inversion converge to the true solution, where dispersion curves act as a smoothness constraint by averaging the shear velocities at different depth ranges. To study the influence of the initial model in the inversion, we carried out joint inversion for station AMT, using different initial models (Fig. 13). We performed inversion with ak135 (Kennett *et al.* 1995, blue line) and iasp91 (Kennett & Engdahl 1991, green line) velocity model, keeping Moho fixed at 40 km with layer thicknesses 2 km down to a depth of 40 km and 5 km below it to a depth of 200 km. We also use the similar initial model (magenta line) used by Julià *et al.* (2009) that consists of a 40-km-thick crust with linear increase in *S*-wave velocity from 3.4 to 4.0 $\mathrm{km\,s^{-1}}$ overlying a flattened PREM model (Dziewonski & Anderson 1981) down to a depth of 200 km. Inversion is repeated 20 times to have final models. These models are compared with our final models (red line). All the models fit the dispersion data (Fig. 13b) and receiver function (Fig. 13c) very well and converge to the similar final model (Fig. 13a).

The resulting velocity models are discussed with reference to continental crust of average thickness ∼40 km (Christensen 1996; Rudnick & Gao 2003) divided into upper, middle and lower crust corresponding to depth interval of 0–11, 11–23 and 23–40 km with the corresponding shear velocity of 2.8–3.5, 3.5–3.8, 3.8–4.1 $\mathrm{km\,s^{-1}}$, respectively. Usually the shear velocity (V_s) ∼ 4.0 $\mathrm{km\,s^{-1}}$ and above is considered as the representative for the basal layer and the Moho is defined by a jump in seismic wave velocity to values greater than 7.6–8.0 $\mathrm{km\,s^{-1}}$ for *P* wave and 4.3–4.6 $\mathrm{km\,s^{-1}}$ for *S* wave. For a variety of mafic lower crustal rocks, the shear wave velocity increases to 3.8 $\mathrm{km\,s^{-1}}$ for felsic granulite, to 3.9 $\mathrm{km\,s^{-1}}$ for mafic granulite, to >4.1 $\mathrm{km\,s^{-1}}$ for garnet granulite rocks. Using this methodology, thickness of the upper, middle, lower, basal layer and the average V_s of the crust are calculated. The similar methodology is applied for all the stations of the Dharwar Craton.

7 RESULTS

In Fig. 14, we present the shear velocity results for representative stations in different tectonic blocks namely: EDC, CG, WDC, Western Ghat, SGT and Eastern Ghat. Each plot of Figs 14(a) and (b) represent the synthetic group velocity dispersion curve and synthetic receiver function (red lines), respectively, corresponding to the shear velocity model in Fig. 14(c), which fit the observed group velocities (black and red circles) and observed receiver function (blue line) very well. Due to poor quality and severe complexity in receiver functions, we are unable to invert receiver functions for stations PDC, TDT and VBD. These stations are not included in our analysis. The velocity models for all other stations are presented in Fig. S2. Important results obtained from those models are summarized in Table S1.

To access the reliability of the velocity-depth image (down to 55 km depth) obtained in this study, 1-D shear velocity inversion

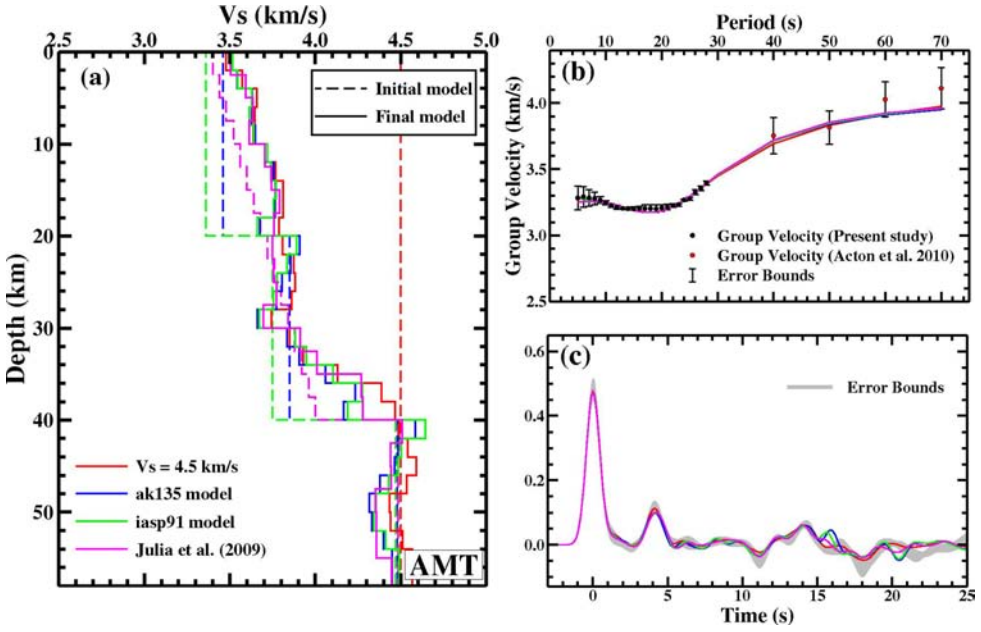

Figure 13. Effect of different initial models on inversion results. (a) Initial (dashed lines) and final (thick lines) models corresponding to the $V_s = 4.5\,\mathrm{km\,s^{-1}}$ (present study), ak135 model (Kennett *et al.* 1995), iasp91 model (Kennett & Engdahl 1991) and Julià *et al.* (2009) model. (b) Fitting of dispersion curves (coloured lines) and observed group velocities (black and red circles) with error bars corresponding to the models in (a). (c) Fitting synthetic receiver functions (coloured lines) with error bounds (grey lines) corresponding to the models in (a).

results are compared with those from previous studies obtained using joint inversion of receiver function and surface wave velocities from earthquake waveforms (Rai *et al.* 2003; Julià *et al.* 2009) and receiver function inversion results (Sarkar *et al.* 2003; Fig. 15). Comparison shows similar crustal structure for most of the stations. Differences occur in the upper crust velocity image at few stations (like DHR, HSN) which may be due to the inclusion of group velocity dispersion data at lower periods providing better control at shallow depth compared to earlier studies.

Shear velocity maps at different depth ranges are presented in Fig. 16. These maps are created by interpolating the 1-D shear velocity model in 10 × 10 km grid obtained from each of the stations of the Dharwar Craton and then average them in that selected depth ranges. Map shows the existence of upper crust down to a depth of 4 km. In 4–10 km depth range, few stations of greenstone belt show velocity corresponding to lower crustal velocity ($V_s > 3.8\,\mathrm{km\,s^{-1}}$). The middle crust ($V_s \sim 3.5$–$3.8\,\mathrm{km\,s^{-1}}$) is mapped to ∼10–20 km depth ranges. In 20–34 km depth ranges most part of the craton enters in the lower crust. At 34–40 km depth, $V_s \geq 4.0\,\mathrm{km\,s^{-1}}$ is observed for most part of the WDC, SGT and Western Ghat which continues to 40–50 km depth ranges. Since, Moho depth in the EDC is ∼35 km, it reaches the mantle at 34–40 km depth ranges. Considering that the Moho beneath the EDC is at ∼35 km while beneath the WDC and SGT it is ∼38–52 km, mafic lower most crust ($V_s \geq 4.0\,\mathrm{km\,s^{-1}}$) is inferred to be very thin (<4 km) beneath the EDC as compared to a thicker (∼20 km) column beneath the WDC and SGT. In 40–50 km depth ranges, entire Dharwar Craton enters in the mantle, except greenstone belt where thickest Moho depth is observed (∼52 km).

7.1 Comparison with global Precambrian velocity models

We compare the velocity character of the Archean and Proterozoic crust in the Dharwar Craton with those derived for global average (Fig. 17). The shear velocity model representing the global Precambrian crust (Fig. 18) is computed from the compilation of global *P*-wave velocity model (Christensen & Mooney 1995) using the average V_p/V_s ratio for the crust computed using crustal petrology model (Christensen 1996). Based on the geology, stations are grouped and their average velocity–depth profile is created along with the deviation. Stations in EDC, CG and CB have $V_s \sim 3.5$–$3.7\,\mathrm{km\,s^{-1}}$ in the upper 10 km, followed by $3.8\,\mathrm{km\,s^{-1}}$ in the depth of 10–32 km. Moho is mapped at ∼36 km. The WDC has similar velocity like the EDC down to a depth of ∼24 km. Beyond this depth the velocity increases and reaches $\sim 4.0\,\mathrm{km\,s^{-1}}$ at ∼32 km. Average Moho depth in the WDC is ∼44 km with about 12 km of mafic cumulate ($V_p \sim 7.0\,\mathrm{km\,s^{-1}}$) above the Moho. In SGT, we observe larger scatter in velocity to a depth of 5 km beyond which it is similar to those observed beneath the WDC. Similar observations are made for Eastern and Western Ghat stations. It may be noted that the EDC has velocity character similar to the global average while for other terrains; shear velocity in lower crust is significantly higher compared to the global velocity model.

7.2 Moho depth and average crust velocity

The data obtained from joint inversion modelling are interpolated over a 10 × 10 km grid to generate Moho depth variation map of the region. We also plot the surface topography of the region (Fig. 19a). The Moho depth map (Fig. 19b) shows a clear division of the WDC, in the north WDC and south WDC. Within the WDC, we observe variations in Moho depth: 42–46 km in north, 48–52 km in south and thinned Moho (∼38–42 km) in central part. This is possibly the first clear distinction observed between the north and south WDC which are known to be of distinct Archean ages and lithology. The SGT can be separated in two blocks; West SGT (Moho depth ∼49 km) and East SGT (Moho depth ∼41 km). For other tectonic blocks Moho depth varies from 34–38 km in the EDC, 42–46 km in Western Ghat, ∼38–46 km in Eastern Ghat, 36 km in CB and 40 km in CG. The EDC is characterized by an elevation of 400–800 m (Fig. 19a) and

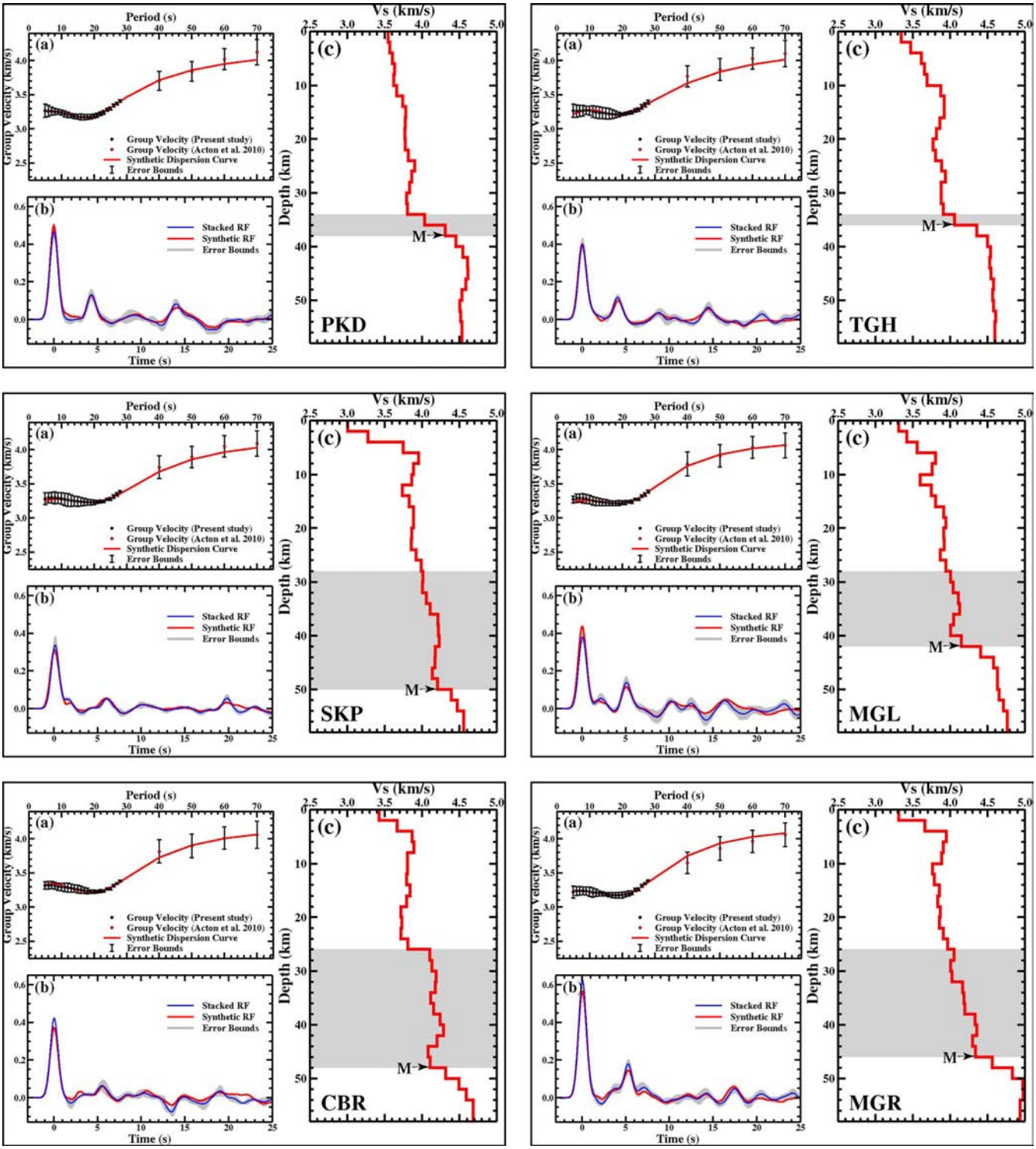

Figure 14. Joint inversion results. (a) Fitting of dispersion curve (red line) with observed group velocities (black and red circles) with error bars. (b) Fitting of stacked receiver function (blue line) with synthetic receiver function (red line) and error bounds (grey lines). (c) Shear velocity model (station name plotted at the bottom left-hand corner of the plot). M denotes the Moho discontinuity and grey shaded region denotes the thickness of the basal layer ($V_s \geq 4.0\,\mathrm{km\,s^{-1}}$).

Moho depth of 34–38 km. Despite having similar topography as of the EDC, the WDC shows large variation in the Moho depth: 42–46 km in north to 48–52 km in its south. Using normal density contrast across Moho, this should lead to an elevation of more than 3 km in the southern part of the WDC. However, in view of the nearly flat topography (∼600 m) in this region, we speculate that this region is compensated by high-density (and high-velocity) material in the lowermost crust. The granulite terrain (SGT) and Eastern and Western Ghats have Moho depth of ∼44 km (average). Corresponding to the Moho depth discussed earlier, we compute the average shear velocity of the crust and present in Fig. 19(c). The average V_s for the EDC is mostly 3.70–3.78 $\mathrm{km\,s^{-1}}$, significantly

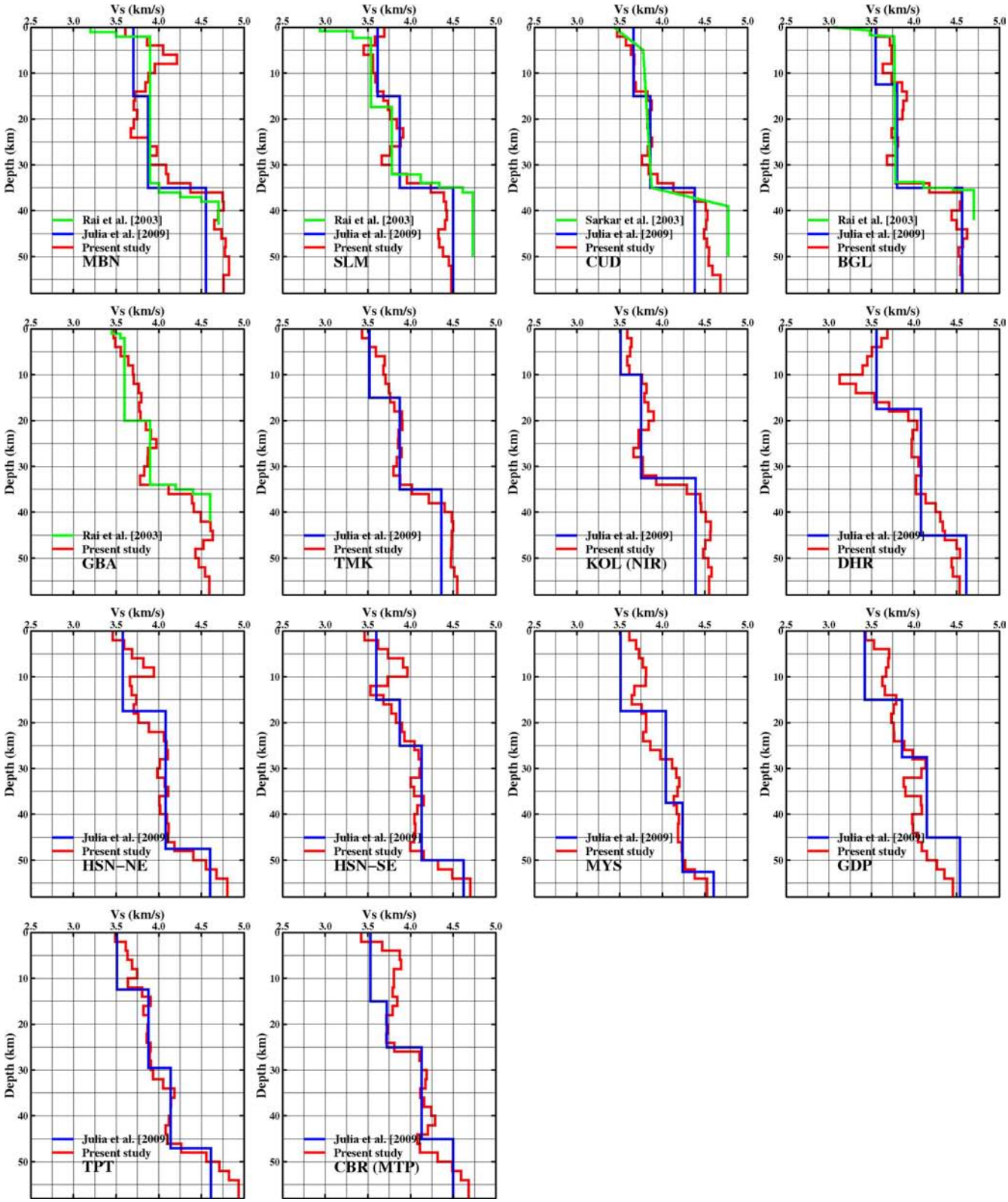

Figure 15. Comparison of shear velocity models between this study (red line) with other earlier studies (e.g. Rai *et al.* 2003; Sarkar *et al.* 2003; Julià *et al.* 2009).

lower (and felsic-intermediate) as compared to the WDC (mostly 3.80–3.95 km s^{-1}) that is more mafic in nature. Like the WDC, stations that belong to the SGT, Eastern Ghat and Western Ghat show high average crustal V_s (~3.86 km s^{-1}).

7.3 Nature of the lower continental crust

From the resultant shear velocity model, we compute the thickness and velocity of the lower crust (Figs 20a and b). Thickness of the

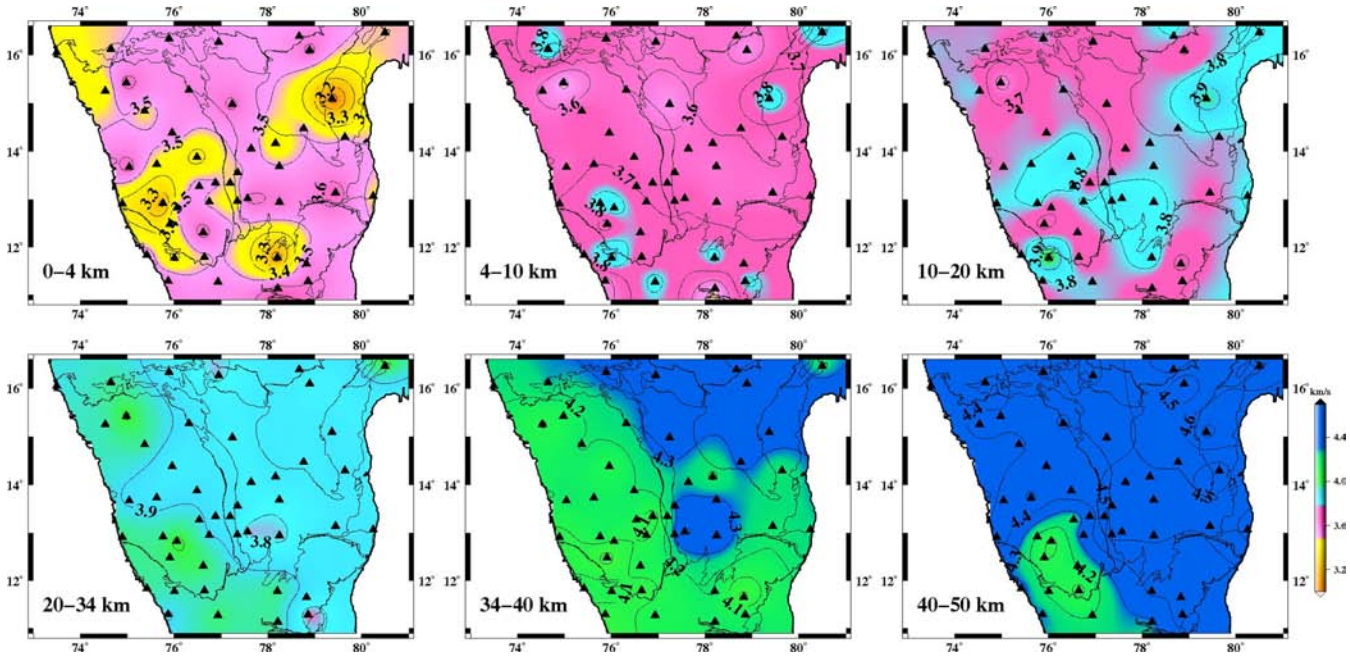

Figure 16. Shear velocity variation map at different depth ranges. Stations (black triangle) and tectonic boundaries (black solid line) are projected on each plot.

lower crust beneath the EDC is on average around ∼12 km, except in the central part where it is ∼18 km (PKD and KDR station; Table S1). Stations within and in the neighbourhood of CG have thicker lower crust (∼20 km) compared to the other EDC stations. Thickness of the lower crust beneath the WDC, SGT and Eastern and Western Ghat varies between 20 and 30 km (Fig. 20a). The average lower crust velocity is ∼3.95 km s^{-1} except in the greenstone belt and the granulite terrain, where it is in the range of ∼4–4.1 km s^{-1} (Fig. 20b).

7.4 The lowermost crust

To study the variable character of the lowermost crust and the nature of crust–mantle interaction, we map the layer with $V_s \geq 4.0$ km s^{-1} (basal layer). Thickness of the basal layer is plotted in Fig. 20(c). Thickness of the basal layer is indicative of the sharpness of Moho. In the lowermost crust, the EDC is quite distinct from the other tectonic blocks. The basal layer thickness is on average ∼5 km in the EDC, 10–16 km beneath most part of the WDC except the mid-Archean greenstone belt, where it is ∼22–27 km. Thickness of the basal layer in western SGT is more (∼20 km) compared to the eastern part (∼7 km). The study suggests that Moho is relatively a thin transition beneath the EDC compared to the WDC. Also, we observe similar segmentation in SGT between the east and west. Considering that there is little difference in both the topography and the Bouguer gravity field in the study region, we speculate that the lowermost crust has high-density mafic/ultramafic composition in the WDC and SGT.

8 DISCUSSIONS AND CONCLUSIONS

We compute cross-correlation of 18 months long time-series of ambient seismic noise recorded on 35 broad-band seismographs operated during 2009 February to 2010 August over the Dharwar Craton and adjoining granulite terrain to produce the interstation Rayleigh-wave group velocity (5–28 s periods) measurements. The number of paths varies from 308 to 488 depending on the period of group velocity. These measurements are transformed into group velocity maps. This is supplemented with the longer period group velocity data (40–70 s) from Acton *et al.* (2010) and then jointly inverted with receiver function data to produce 3-D shear velocity depth image of the study region. Significant findings of the shear wave velocity image reconstructed from joint inversion results of the dispersion data and receiver function modelling include the following:

(1) Short period (5–10 s) Rayleigh-wave tomographic images show an excellent correlation with the surface geology where Archean and Proterozoic basins have lower group velocity (3.15–3.25 km s^{-1}) compared to exposed mid-lower crust terrains with higher group velocity (3.25–3.40 km s^{-1}). Also most of the schist belts are characterized by higher group velocity (3.3–3.4 km s^{-1}).

(2) The Dharwar Craton, despite being a predominantly Archean terrain, has significant lateral variability in Moho depth. Some of the features include: a nearly flat Moho at a depth of 34–38 km beneath the EDC, and Moho at a depth of 42–54 km in the WDC. The deepest Moho is observed beneath the greenstone belt in southern part of the WDC where vestiges of early-mid Archean (∼3.36 Ma) enclaves are found. Moho depths for other tectonics blocks vary from 40 to 50 km in SGT, 42 to 46 in Western Ghat, 38 to 46 km in Eastern Ghat, 36 km in CB and 40 km in CG. The Moho depth changes by over 10 km are unusual in continents (Jackson *et al.* 2008). It is important to understand the geological process responsible for preservation of such a Moho configuration. Meissner & Kusznier (1987) based on rheological studies suggest the existence of high strength layer in the uppermost mantle. A number of researchers have examined the longevity of such Moho topography (Housman *et al.* 1981; Meissner & Kuszir 1987; Kusznir & Mathew 1988). They suggest lower crustal flow can remove all but long- and

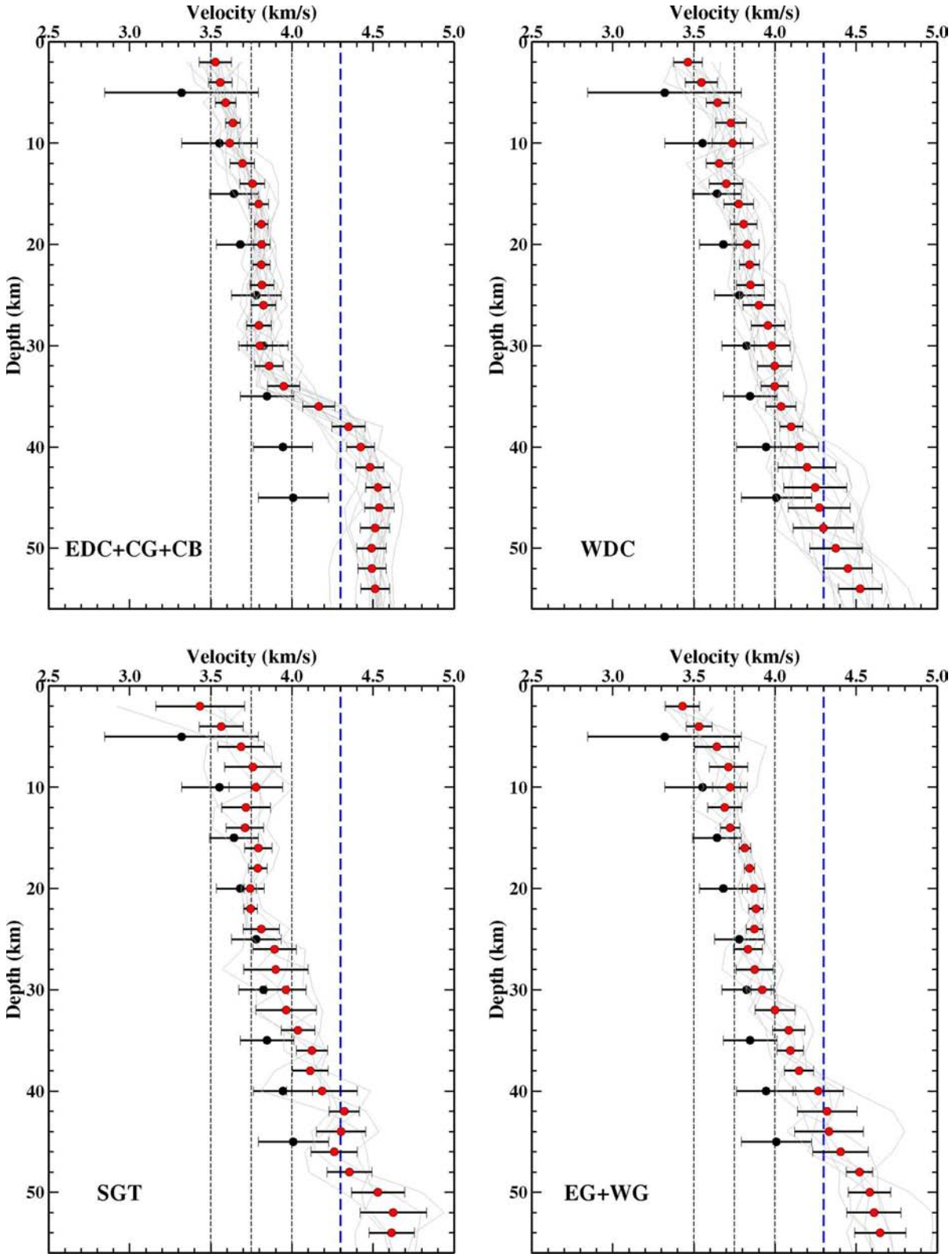

Figure 17. Comparison of the shear velocity character of the Archean and Proterozoic crust in the Dharwar Craton with those derived for global average (black circles) with error bar. Red circles are the average shear velocity model calculated from the shear velocity models (grey curves) with error bar, obtained from the tectonic blocks (bottom left corner) at every 2 km. Black dashed lines are marked at 3.5 (marker for upper-middle crust), 3.75 (average of 3.5 and 4.0) and 4.0 km s^{-1} (marker for basal layer). Blue dashed line is marked at 4.3 km s^{-1} to identify Moho.

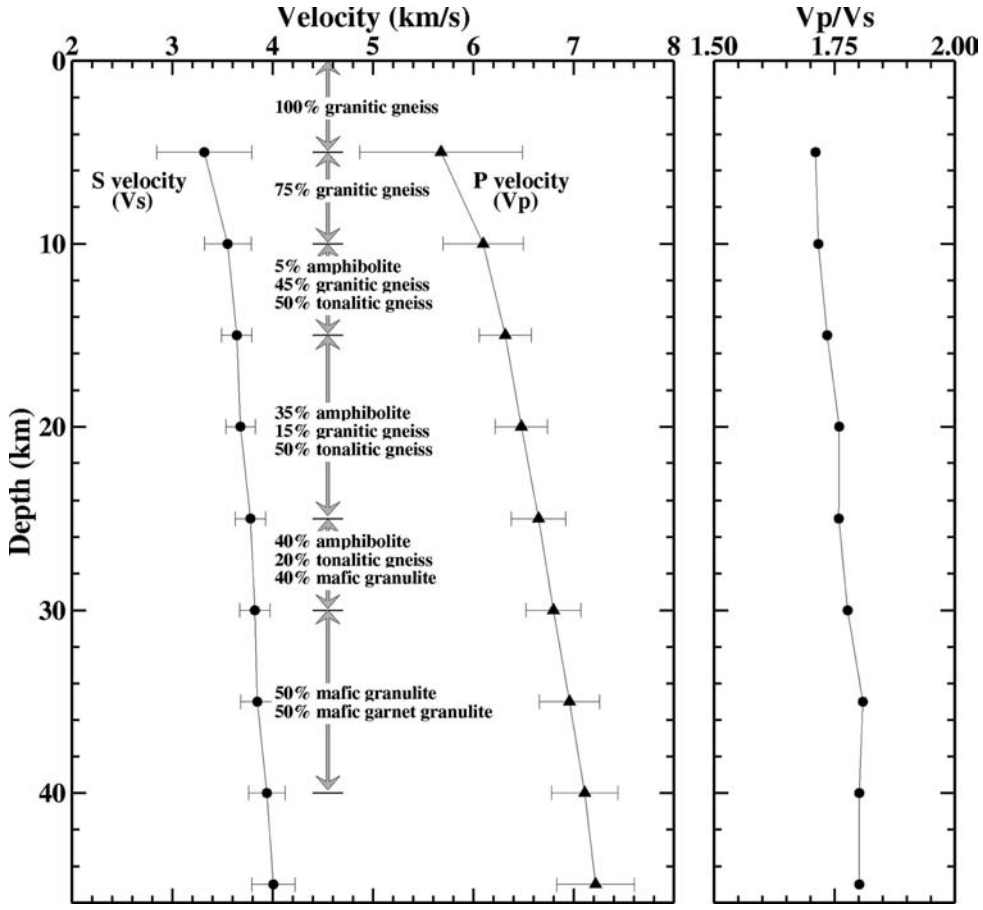

Figure 18. The shear velocity model representing the global Precambrian crust computed from the compilation of global *P*-wave velocity model (Christensen & Mooney 1995) and using the average V_p/V_s ratio computed from crustal petrology model (Christensen 1996).

short-wavelength Moho topography and hence possibly some of the Precambrian Moho topographies may survive (McKenzie *et al.* 2000).

(3) Lower crust beneath the EDC is thinner as compared to thicker one beneath the WDC, Eastern and Western Ghat and SGT where it varies from ∼20 to 30 km. Stations situated on and close to the K-rich mantle-derived CG also have thick lower crust (∼20 km). We observe a thin mafic layer (<5 km) above Moho beneath the EDC compared to a thick layer (∼10–27 km) beneath the southern part of the WDC. Data from the EDC are consistent with the studies over most of the late Archean cratons of America, Africa and Australia (e.g. Durrheim & Mooney 1994; Chevrot & van der Hilst 2000; Niu & James 2002; Reading *et al.* 2007). Our observation of significant mafic cumulate beneath the mid-Archean WDC is at odd with the models of crustal evolution (Nelson 1991). Underplating of magma is commonly associated with the formation of a residual mafic layer in lower crust characterized by high velocity and could explain the evolution of cratons like Karelia (Peltonen *et al.* 2006), North China west block (Zhang *et al.* 2012). We argue that under higher thermal gradient during Archean, tectonically buried oceanic crust in presence of water would have been converted to highly mafic crust that would have been strong and too buoyant to sink into the mantle (Bjornereud & Austrheim 2004). We speculate presence of partially eclogitized rocks in the lower crust of the WDC.

(4) The average crustal velocity in most part of the EDC is ∼3.75 km s^{-1}, suggestive of its intermediate composition as also hypothesized based on geochemical measurements (Chadwick *et al.* 2000) compared to 3.80–3.95 km s^{-1} in the WDC. It, however, remains an open issue when and how the EDC crust turned to be intermediate in composition from a more primitive basalt composition. This differentiation has been explained as due to lower crust foundering (Kay & Kay 1991) or through a process of crustal relamination (Hacker *et al.* 2011) as a possible consequence of subduction of the WDC beneath the EDC. The process of delamination of the EDC lower crust finds support from presence of eclogites in the xenoliths at the margin of WDC/EDC. We speculate that the delamination process could have been responsible for a nearly flat Moho and felsic-intermediate composition of the crust beneath the EDC.

ACKNOWLEDGEMENTS

The research is supported by CSIR–NGRI project India Deep Earth Exploration (INDEX) and JC Bose research grant to SSR. KB was supported by a research fellowship from the CSIR. We are grateful to Nick Rawlinson for providing us the FMST code. We greatly appreciate help of K. Sivaram, K. Nagaraju, P. Mahesh, V. Pavan Kumar and Gyan Singh Meena during the field deployment of seismographs. Most of the data processing was made using Seismic

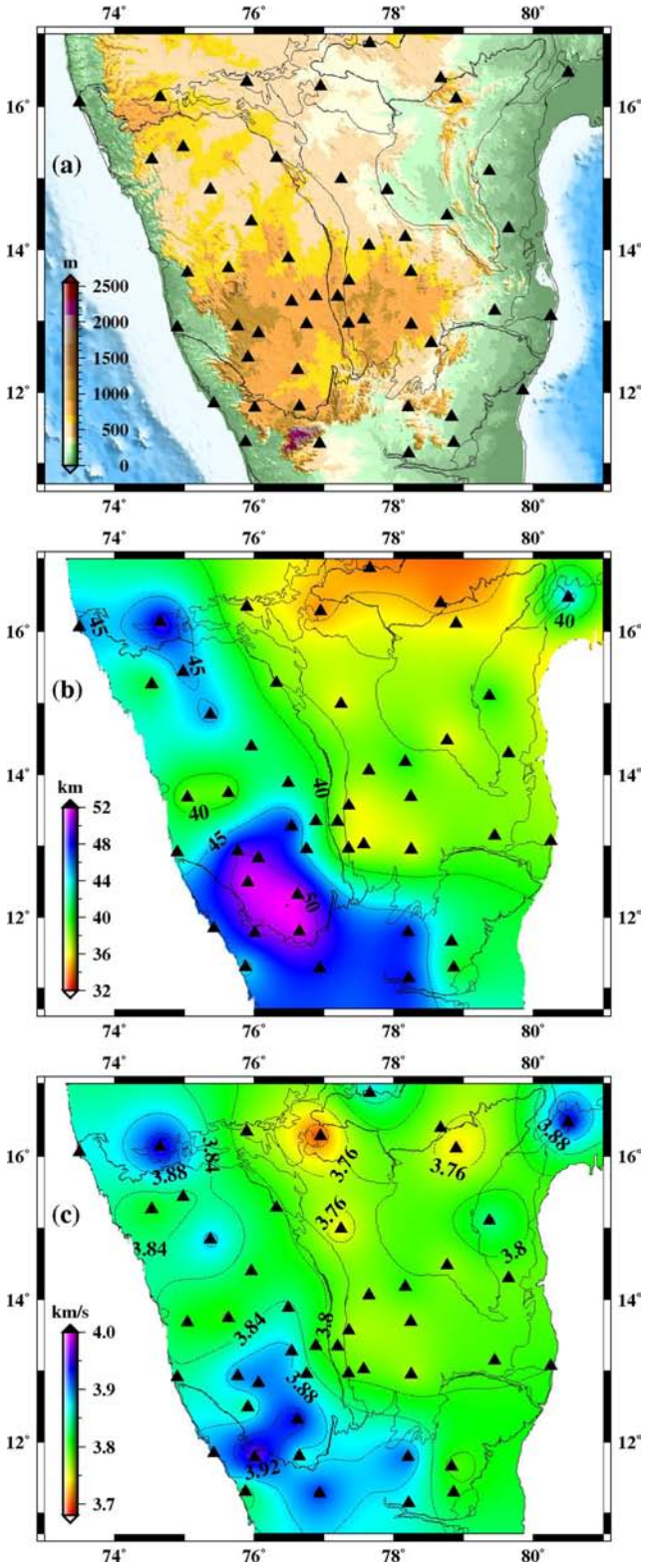

Figure 19. (a) Topography and (b) Moho depth variation map of the study region. Contours are plotted at every 5 km by dashed lines. (c) Average shear velocity variation map. Other details are same as in Fig. 16.

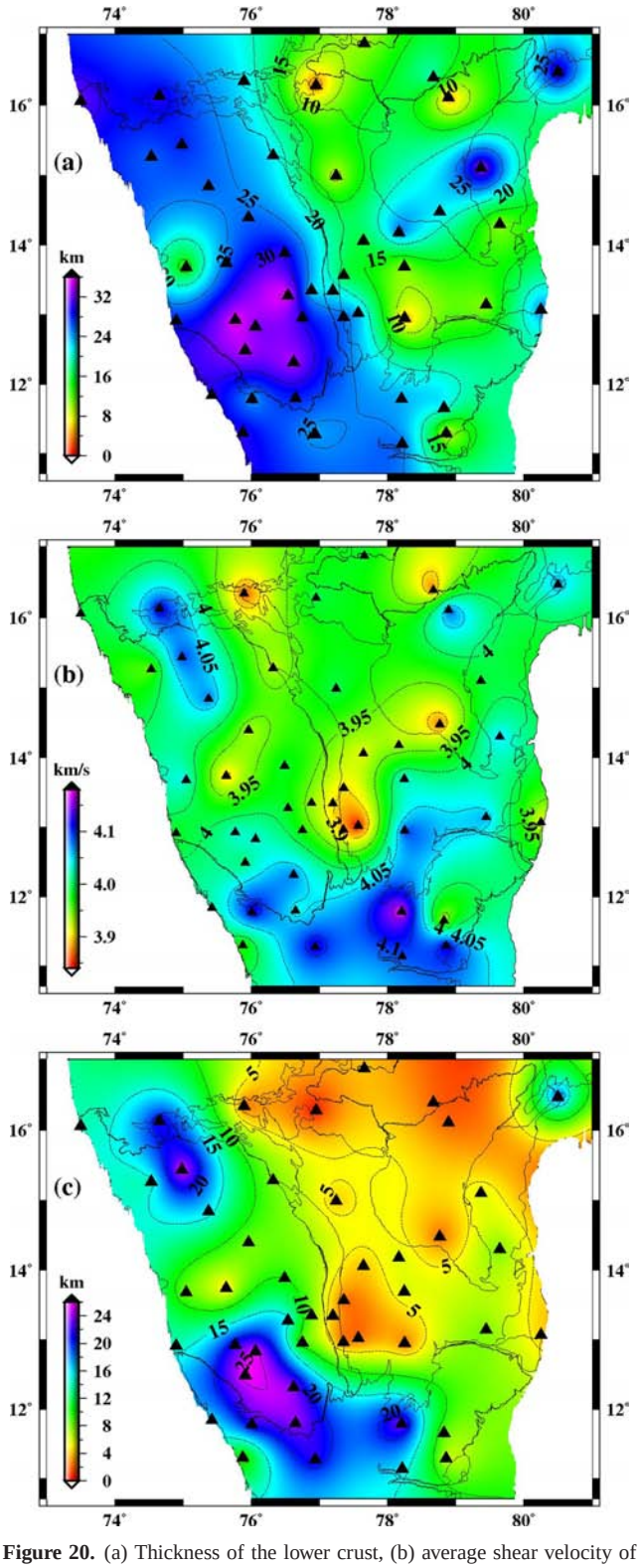

Figure 20. (a) Thickness of the lower crust, (b) average shear velocity of the lower crust and (c) thickness of the basal layer of the crust in the south Indian shield. Other details are same as in Fig. 16.

Analysis Code (SAC) and figures were made using Generic Mapping Tools (GMT; Wessel & Smith 1998). We thank the Editor Mike Ritzwoller and both the reviewers (Jordi Julià and anonymous) for their valuable suggestions for improving the paper.

REFERENCES

Acton, C.E., Priestley, K., Gaur, V.K. & Rai, S.S., 2010. Group velocity tomography of the Indo-Eurasian collision zone, *J. geophys Res.*, **115,** B12335, doi:10.1029/2009JB007021.

Ammon, C.J., 1991. The isolation of receiver effects from teleseismic P waveforms, *Bull. seism. Soc. Am.*, **81,** 2504–2510.

Ammon, C.J., Randall, G.E. & Zandt, G., 1990. On the nonuniqueness of receiver function inversions, *J. geophys. Res.*, **95,** 15 303–15 318.

Artemieva, I.M. & Meissner, R., 2012. Crustal thickness controlled by plate tectonics: a review of crust-mantle interaction process illustrated by European examples, *Tectonophysics*, **530–531,** 18–49.

Bensen, G.D., Ritzwoller, M.H., Barmin, M.P., Levshin, A.L., Lin, F., Moshetti, M.P., Shapiro, N.M. & Yang, Y., 2007. Processing seismic ambient noise data to obtain reliable broad-band surface wave dispersion measurements, *Geophys. J. Int.*, **169,** 1239–1260.

Bensen, G.D., Ritzwoller, M.H. & Shapiro, N.M., 2008. Broadband ambient noise surface wave tomography across the United States, *J. geophys. Res.*, **113,** B05306, doi:10.1029/2007JB005248.

Bjornerud, M.G. & Austrheim, H., 2004. Inhibited eclogite formation: the key to the rapid growth of strong and bouyant Archean continental crust, *Geology*, **32,** 765–768.

Bouhallier, H., Chardon, D. & Choukroune, P., 1995. Strain patterns in Archaean dome and basin structures: the Dharwar craton (south India), *Earth planet. Sci. Lett.*, **135,** 57–75.

Bostock, M.G. & Rondenay, S., 1999. Migration of scattered teleseismic body waves, *Geophys. J. Int.*, **137,** 732–746.

Chadwick, B., Vasudev, V.N. & Hedge, G.V., 2000. The Dharwar craton, south India interpreted as the result of late Archaean oblique convergence, *Precambrian Res.*, **99,** 91–111.

Chevrot, S. & van der Hilst, R.D., 2000. The Poisson's ratio of the Australian crust: geological and geophysical implications, *Earth planet. Sci. Lett.*, **183,** 121–132.

Christensen, N.I., 1996. Poisson's ratio and crustal seismology, *J. geophys. Res.*, **101,** 3139–3156.

Christensen, N.I. & Mooney, W.D., 1995. Seismic velocity structure and composition of the continental crust: a global view, *J. geophys. Res.*, **100,** 9761–9788.

Collins, C.D.N., 1991. Nature of the crust-mantle boundary under Australia from seismic evidence, *Geol. Soc. Australia Spec. Publ.*, **17,** 67–80.

Derode, A., Larose, E., Tanter, M., de Rosny, J., Tourim, A., Campillo, M. & Fink, M., 2003. Recovering the Green's function from filed-field correlations in an open scattering medium (L), *J. acoust. Soc. Am.*, **113,** 2973–2976.

Diaconescu, C.C., Knapp, J.H., Brown, L.D., Steer, D.N. & Stiller, M., 1998. Precambrian Moho offset and tectonic stability of the East European platform, *Geology*, **26,** 211–214.

Drury, S.A., Harris, N.B., Holt, R.W., Reeves-Smith, G.J & Wightman, R.T., 1984. Precambrian tectonics and crustal evolution in south India, *J. Geol.*, **92,** 3–20.

Durrheim, R.J. & Mooney, W.D., 1994. Evolution of the Precambrian lithosphere: seismological and geochemical constraints, *J. geophys. Res.*, **99,** 15 359–15 374.

Dziewonski, A.M. & Anderson, D.L., 1981. Preliminary reference Earth model, *Phys. Earth planet. Inter.*, **25,** 297–356.

Dziewonski, A.M., Bloch, S. & Landisman, M., 1969. A technique for the analysis of transient seismic signals, *Bull. seism. Soc. Am.*, **59,** 427–444.

Gaur, V.K. & Priestley, K.F., 1996. Shear wave velocity structure beneath the Archaean granites around Hyderabad inferred from receiver function analysis, *Proc. Ind. Acad. Sci. (E&P)*, **105,** 1–8.

Griffin, W.L. & O'Reilly, S.Y., 1987. Is the continental Moho the crust-mantle boundary? *Geology*, **15,** 241–244.

Gupta, S., Rai, S.S., Prakasam, K.S., Srinagesh, D., Bansal, B.K., Chadha, R.K., Pristley, K. & Gaur, V.K, 2003a. The nature of the crust in southern India: implication for Precambrian crustal evaluation, *Geophys. Res. Lett.*, **30**, doi:10.1029/2002GL016770.

Gupta, S., Rai, S.S., Prakasam, K.S., Srinagesh, D., Chadha, R.K., Prisetley, K. & Gaur, V.K, 2003b. First evidence for anomalous thick crust beneath mid-Archean western Dharwar craton, *Curr. Sci.*, **84,** 1219–1226.

Hacker, B.H., Kelemen, P.B. & Behn, M.D., 2011. Differentiation of the continental crust by relamination, *Earth planet. Sci. Lett.*, **307,** 501–516.

Hawkesworth, C.J. & Kemp, A.I.S, 2006. Evolution of the continental crust, *Nature*, **443,** 811–817.

Herrmann, R.B., 1973. Some aspects for band-pass filtering of surface waves, *Bull. seism. Soc. Am.*, **63**(2), 663–671.

Herrmann, R.B. & Ammon, C.J., 2004. *Surface Wave, Receiver Function and Crustal Structure*. Computer Programs in Seismology, Version 3.30, St. Louis University.

Housman, G.A., McKenzie, D.P. & Molnar, P, 1981. Convective instability of a thickened boundary layer and its relevance for the thermal evolution of continental convergent belts, *J. geophys. Res.*, **86,** 6115–6132.

Jackson, J., Mckenzie, D., Priestley, K.F. & Emerson, B., 2008. New views on the rheology and structutre of the lithosphere, *J. Geol. Soc. Lond.*, **165,** 453–465.

Jagadeesh, S. & Rai, S.S., 2008. Thickness, composition and evolution of the Indian Precambrian crust, *Precambrian Res.*, **162,** 4–15.

Julià, J., Ammon, C.J., Herrmann, R.B & Correig, A.M., 2000. Joint inversion of receiver function and surface wave dispersion observations, *Geophys. J. Int.*, **143,** 99–112.

Julià, J., Jagadeesh, S., Rai, S.S. & Owens, T.J., 2009. Deep crustal structure of the Indian Shield from joint inversion of P-wave receiver functions and Rayleigh-wave group velocities: implications for Precambrian evolution, *J. geophys. Res.*, **114**, doi:10.1029/2008JB006261.

Kaila, K.L. & Bhatia, S.C., 1981. Gravity study along Kavali-Udipi deep seismic sounding profile in the Indian peninsular shield: some inferences about origin of anorthosites and Eastern Ghat Orogeny, *Tectonophysics*, **79,** 129–143.

Kaila, K.L. & Krishna, V.G., 1992. Deep seismic sounding studies in India and major discoveries, in *Seismology in India: An Overview (Spl. Issue, Curr. Sci.)*, Vol. **62,** pp. 117–154, eds Gupta, H.K. & Ramaseshan, S., Indian Academy of Sciences.

Kaila, K.L. *et al.*, 1979. Crustal structure along Kavari-Udipi profile in the Indian peninsular shield from deep seismic soundings, *J. Geol. Soc. Ind.*, **20,** 307–333.

Kay, R.W. & Kay, S.M., 1991. Creation and destruction of lower continental crust, *Geol. Rundsch.*, **80,** 1–20.

Kennett, B.L.N. & Engdahl, E.R., 1991. Traveltimes for global earthquake location and phase identification, *Geophys. J. Int.*, **105**(2), 429–465.

Kennett, B.L.N., Sambridge, M. & Williamson, P.R., 1988. Subspace methods for large scale inverse problems involving multiple parameter classes, *Geophys. J. Int.*, **94,** 237–247.

Kennett, B.L.N., Engdahl, E.R. & Bulland, R., 1995. Constraints on seismic velocities in the Earth from travel times, *Geophys. J. Int.*, **122,** 108–124.

Kiselev, S., Vinnik, L., Oreshin, S., Gupta, S., Rai, S.S., Singh, A., Kumar, M.R. & Mohan, G., 2008. Lithosphere of the Dharwar craton by joint inversion of P and s receiver functions, *Geophys. J. Int.*, **173**(3), 1106–1118.

Korenaga, J. & Kelemen, P.B., 1997. Origin of gabbro sills in the Moho transition zone of the Oman ophiolite: implication for magma transport in the oceanic lower crust, *J. geophys. Res.*, **102,** 27 729–27 749.

Krishna, V.G. & Ramesh, D.S., 2000. Propagation of crustal-waveguide-trapped Pg and seismic velocity structure in the south Indian shield, *Bull. seism. Soc. Am.*, **90,** 1281–1294.

Kusznir, N.J. & Matthews, D.H., 1988. Deep seismic reflections and deformational mechanics of the continental lithosphere, *J. Petrol.*, Special Lithosphere issue (1), 63–87.

Langston, C.A., 1977. Corvallis, Oregon, crustal and upper mantle structure from teleseismic P and S waves, *Bull. seism. Soc. Am.*, **67,** 713–724.

Larose, E., Derode, A., Corennec, D., Margerin, L. & Campillo, M., 2005. Passive retrieval of Rayleigh waves in discovered elastic media, *Phys. Rev. E.*, **72,** doi:10.113/PhysRevE.72.046607.

Liang, C. & Langston, C.A., 2008. Ambient seismic noise tomography and structure of northeastern America, *J. geophys. Res.*, **113,** doi:10.1029/2007/JB005350.

Ligorría, J.P. & Ammon, C.J., 1999. Iterative deconvolution and receiver-function estimation, *Bull. seism. Soc. Am.*, **358,** 233–265.

Lin, F.C., Ritzwoller, M.H., Townend, J., Bannister, S. & Savage, M.K., 2007. Ambient noise Rayleigh wave tomography of New Zealand, *Geophys. J. Int.*, **170**(2), 649–666.

McBride, J.H., 1995. Does the great Glen fault really disrupt Moho and upper mantle structure, *Tectonics*, **14,** 422–434.

McKenzie, D., Nimmo, F., Jackson, J.A., Gans, P.B. & Miller, E.L., 2000. Characteristics and consequences of flow in the lower crust, *J. geophys. Res.*, **105,** 11 029–11 046.
Meissner, R. & Kuszir, N., 1987. Crustal viscocity and the reflectivity of the lower crust, *Ann. Geophys.*, **5B,** 365–373.
Mengel, K. & Kern, H., 1992. Evolution of petrological and seismic Moho-implication for the continental crust-mantle boundary, *Terra Nova*, **4,** 109–116.
Mitra, S., Priestley, K., Gaur, V.K. & Rai, S.S., 2006. Shear wave velocity structure of the south Indian lithosphere from Rayleigh wave phase velocity measurements, *Bull. seism. Soc. Am.*, **96,** 1551–1559.
Mjelde, R., Goncharov, A. & Muller, R.D., 2013. The Moho: boundary above upper mantle peridotites or lower crustal eclogites? A global review and new interpretations for passive margins, *Tectonophysics* **609,** 636–650.
Mottaghi, A.A., Rezapour, M. & Korn, M., 2013, Ambient noise surface wave tomography of the Iranian Plateau, *Geophys. J. Int.*, **193,** 452–462 .
Nagaraja Rao, B.K., Rajurkar, S.T., Ramlingaswami, G. & Ravindra Babu, B., 1987. Stratigraphy, structure and evolution of Cuddapah basin, Dharwar Craton, *Mem. Geolog. Soc. Ind.*, **6,** 33–86.
Naqvi, S.M. & Rogers, J.J.W., 1996. *Precambrian Geology of India*, Clarendon Press.
Nelson, K.D., 1991. A unified view of craton evolution motivated by recent deep seismic reflection and refraction results, *Geophys. J. Int.*, **105**(1), 25–35.
Niu, F. & James, D.E., 2002. Fine structure of the lowermost crust beneath the Kaapvaal craton and its implications for crustal formation and evolution, *Earth planet Sci. Lett.*, **200,** 121–130.
Olafsson, I., Sundvor, E., Eldholm, O. & Grue, K., 1992. More Margin: crustal structure from the analysis of expanded spread profile, *Mar. geophys. Res.*, **14,** 137–162.
Pasyanos, M.E., 2005. A variable resolution surface wave dispersion study of Eurasia, North Africa, and surrounding regions, *J. geophys, Res.*, **110,** B12301. doi:10.1029/2005JB003749.
Pawlak, A., Eaton, D.W., Bastow, I.D., Kendall, J.-M., Helffrich, G., Wookey, J. & Snyder, D., 2011. Crustal structure beneath Hudson Bay from ambient-noise tomography: implications for basin formation, *Geophys. J. Int.*, **184,** 65–82.
Peltonen, P., Manttari, I., Huhma, H. & Whitehouse, M.J., 2006. Multistage origin of the lower crust of the Karelian craton from 3.5 to 1.7 Ga based on isotopic and ages of kimberlite derived mafic granulite xenoith, *Precambrian Res.*, **147,** 107–123.
Rai, S.S., Priestley, K., Prakasam, K.S., Srinagesh, D., Gaur, V.K. & Du, Z., 2003. Crustal shear velocity structure of the south Indian shield, *J. geophys. Res.*, **108**(B2), doi:1029/2002JB001776.
Rawlinson, N. & Sambridge, M., 2004a. Wavefront evolution in strongly heterogeneous layered media using the fast marching method, *Geophys. J. Int.*, **156,** 631–647.
Rawlinson, N. & Sambridge, M., 2004b. Multiple reflection and transmission phases in complex layered media using a multistage fast marching method, *Geophysics*, **69,** 1338–1350.
Reading, A.M., Kennet, B.L.N. & Goleby, B., 2007. New constraints on seismic structure of western Australia: evidence for terrane stabilization prior to the assembly of an ancient continent, *Geology*, **35,** 379–382.
Ritzwoller, M., 2009. Ambient noise seismic imaging, in *McGraw Hill Year Book on Science and Technology*, pp. 1–13, McGraw-Hill.
Roy Chowdhury, K. & Hargraves, R.B., 1981. Deep seismic soundings in India and the origin of continental crust, *Nature*, **291**(**5817),** 648–650.
Rudnick, R.L. & Gao, S., 2003. Composition of the continental crust, in *Treatise on Geochemistry*, Vol. **3,** pp. 1–64, eds Holland, H.D. & Turekian, K.T., Elsevier-Pergamon.
Rychert, A.R., Rondenay, S. & Fischer, K.M., 2007. P-to-S and S-to-P imaging of a sharp lithosphere-asthenosphere boundary beneath eastern North America, *J. geophys. Res.*, **112,** B08314, doi:10.1029/2006JB004619.
Sabra, K.G., Gerstoft, P., Roux, P. & Kuperman, W.A., 2005. Extracting time domain Green's function estimate from ambient noise, *Geophys. Res. Lett.*, **32,** L03310, doi:10.1029/2005GL021862.
Sarkar, D., Kumar, M.R., Saul, J., Kind, R., Raju, P.S., Chadha, R.K. & Shukla, A.K., 2003. A receiver function perspective of Dharwar craton (India) crustal structure, *Geophys. J. Int.*, **154,** 205–211.
Saygin, E. & Kennett, B.L.N., 2012. Crustal structure of Australia from ambient seismic noise tomography, *J. geophys. Res.*, **117,** B01304, doi:10.1029/2011JB008403.
Shapiro, N.M., Campillo, M., Stehly, L. & Ritzwoller, M.H., 2005. High resolution surface wave tomography from ambient seismic noise, *Science*, **307,** 1615–1618.
Snieder, R., 2004. Extracting the Green's function from the correlation of coda waves: a derivation based on stationary phase, *Phys. Rev. E*, **69,** 604–610.
Storey, B.C., 1995. The role of mantle plumes in continental breakup: case histories from Gondwanaland, *Nature*, **377,** 301–308.
Wapenaar, K., 2004. Retrieving the elastodynamic Green's function of an arbitrary inhomogeneous medium by cross correlation, *Phys. Rev. Lett.*, **93,** 254301, doi:10.1103/PhysRevLett.93.254301.
Weaver, R.L. & Lobkis, O.I., 2001. On the emergence of the Green's function in the correlations of a diffuse field, *J. acoust. Soc. Am.*, **110,** 3011–3017.
Wessel, P. & Smith, W.H.F., 1998. New improved version of the Generic Mapping Tools released, *EOS, Trans. Am. geophys. Un.*, **79**, doi:10.1029/98EO00426.
White, R.S., McKenzie, D. & O'Nions, J., 1992. Oceanic crustal thickness from seismic measurements and rare earth element inversion, *J. geophys. Res.*, **97,** 19 683–19 715.
Worthington, J.R., Hacker, B.H., Bradley, R. & Zandt, G., 2013. Distinguishing eclogite from peridotite: EBSD-based calculations of seismic velocities, *Geophys. J. Int.*, **193,** 489–505.
Yang, Y., Ritzwoller, M.H., Levshin, A.L. & Shapiro, N.M., 2007. Ambient noise Rayleigh wave tomography across Europe, *Geophys. J. Int.*, **168,** 259–274.
Yang, Y., Li, A. & Ritzwoller, M., 2008. Crustal and uppermost mantle structure in southern Africa revealed from ambient noise and teleseismic tomography, *Geophys. J. Int.*, **174,** 235–248.
Yao, H., Van der Hilst, R.D. & de Hoop, M.V., 2006. Surface wave tomography of SE Tibet from ambient seismic noise and two station data, *Geophys. J. Int.*, **166,** 732–744.
Zelt, C.A., 1998. Lateral velocity resolution from 3-D seismic refraction data, *Geophys. J. Int.*, **135,** 1101–1112.
Zhang, H.F., Yang, Y.H., Santosh, M., Zhao, X.M. & Xiao, Y., 2012. Evolution of the Archaean and Proterozoic lower crust beneath the Trans-North China Orogen and western block of the North China Craton, *Gondwana Res.*, **22,** 73–85.

SUPPORTING INFORMATION

Additional Supporting Information may be found in the online version of this article:

Table S1. Details of Dharwar network stations, Moho depth, and average shear wave velocity (V_s), thickness of lower crust and basal layer ($V_s \geq 4.0\,\mathrm{km\,s^{-1}}$) used in the analysis.
Figure S1. Checkerboard recoveries for group velocity at different periods (10, 15, 20 and 24 s). Anomalies are plotted with respect to average group velocity (bottom left corner) at that period.
Figure S2. Shear velocity-depth model for all the broad-band seismic stations in different tectonic regions of the study region. Station name is mentioned in bottom-left corner of each plot. M denotes the Moho discontinuity and gray shaded region denote the thickness of the basal layer ($V_s \geq 4.0\,\mathrm{km\,s^{-1}}$) (http://gji.oxfordjournals.org/lookup/suppl/doi:10.1093/gji/ggu075/-/DC1)

Please note: Oxford University Press is not responsible for the content or functionality of any supporting materials supplied by the authors. Any queries (other than missing material) should be directed to the corresponding author for the article.